Elsevier Editorial System(tm) for Combustion and Flame
Manuscript Draft

Manuscript Number:

Title: On Periodic Behavior of Weakly Turbulent Premixed Flame Corrugations

Article Type: Full Length Article

Keywords: Turbulent Premixed Combustion, Proper Orthogonal Decomposition, Symmetric Flame Fronts, V-shaped Flames

Corresponding Author: Mr. Sina Kheirkhah,

Corresponding Author's Institution: University of Toronto Institute for Aerospace Studies

First Author: Sina Kheirkhah

Order of Authors: Sina Kheirkhah; Ömer L Gülder, Ph.D.; Guillaume Maurice, Ph.D.; Fabien Halter, Ph.D.; Iskender Gökalp, Ph.D.

Abstract: Periodicity in evolution of premixed V-shaped flames in the space domain is investigated experimentally. The experiments were performed using the Mie scattering and Particle Image Velocimetry techniques. Three Reynolds numbers of 510, 790, and 1057 along with two fuel-air equivalence ratios of 0.6 and 0.7 were tested in the experiments. The analyses were performed using the Proper Orthogonal Decomposition (POD) technique for the flame front position as well as the velocity data pertaining to non-reacting flow condition. The POD analysis shows that the spectral characteristics of the mode shapes associated with the velocity and the flame front position data feature similarities; however, the corresponding temporal coefficients are significantly different. Specifically, the POD modes shapes pertaining to both velocity and flame front position data feature dominant instabilities. It was shown that the normalized wave number pertaining to these instabilities are similar and equal to the Strouhal number corresponding to non-reacting flow over a circular cylinder. Comparison of the normalized temporal coefficients show that, for the flame front position data, the normalized first and second coefficients are mainly centered close to the origin; however, those associated with the velocity data are positioned around a unity radius circle. This was argued to be linked to the ratio of the corresponding first and second eigenvalues. Specifically, it was shown that, as this ratio approached to unity, the signal energy becomes distributed between the first and the second POD modes. As a result, the normalized temporal coefficients follow a circular pattern.

Suggested Reviewers: Mourad Boukhalfa Ph.D.
CORIA, France
mourad.boukhalfa@coria.fr

Simone Hochgreb Ph.D.
Professor, Engineering department, University of Cambridge
simone.hochgreb@eng.cam.ac.uk

Andrei Lipatnikov Ph.D.
Professor, Applied Mechanics, Chalmers University of Technology
andrei.lipatnikov@chalmers.se

Matthew Johnson Ph.D.
Professor, Mechanical and Aerospace Engineering, Carleton Univerisity
Matthew.Johnson@carleton.ca

On Periodic Behavior of Weakly Turbulent Premixed Flame Corrugations

Sina Kheirkhah[1], Ömer L. Gülder[1], Guillaume Maurice[2], Fabien Halter[2], and Iskender Gökalp[2]

University of Toronto, Institute for Aerospace Studies, 4925 Dufferin Street, Toronto, Ontario, Canada

University of Orléans, CNRS ICARE, Avenue de la Recherche Scientifique, 45072 Orléans Cedex 2 France

Abstract

Periodicity in evolution of premixed V-shaped flames in the space domain is investigated experimentally. The experiments were performed using the Mie scattering and Particle Image Velocimetry techniques. Three Reynolds numbers of 510, 790, and 1057 along with two fuel-air equivalence ratios of 0.6 and 0.7 were tested in the experiments. The analyses were performed using the Proper Orthogonal Decomposition (POD) technique for the flame front position as well as the velocity data pertaining to non-reacting flow condition. The POD analysis shows that the spectral characteristics of the mode shapes associated with the velocity and the flame front position data feature similarities; however, the corresponding temporal coefficients are significantly different. Specifically, the POD modes shapes pertaining to both velocity and flame front position data feature dominant instabilities. It was shown that the normalized wave number pertaining to these instabilities are similar and equal to the Strouhal number corresponding to non-reacting flow over a circular cylinder. Comparison of the normalized temporal coefficients show that, for the flame front position data, the normalized first and second coefficients are mainly centered close to the origin; however, those associated with the velocity data are positioned around a unity radius circle. This was argued to be linked to the ratio of the corresponding first and second eigenvalues. Specifically, it was shown that, as this ratio approached to unity, the signal energy becomes distributed between the first and the second POD modes. As a result, the normalized temporal coefficients follow a circular pattern.

Keywords: Turbulent Premixed Combustion, Proper Orthogonal Decomposition, Symmetric Flame Fronts, and V-shaped Flames

1. Introduction

Several engineering equipment, for example, stationary gas turbines, lean premixed and pre-vaporized jet engines, and spark ignition engines operate under the mode of turbulent premixed combustion [1–3]. Thus, studying this mode of combustion is of significant importance; and, as a result, numerous laboratory settings have been developed to investigate turbulent premixed flames, see, for example, the review papers by [3–5]. These studies show that several flame configurations, e.g., V-shaped, Bunsen-type, swirl-stabilized, spherical, and stagnation, have been utilized to study turbulent premixed flames [3–5]. The flame configuration used in the present study is V-shaped. Previous investigations associated with the V-shaped flames, e.g., [6–8], show that the turbulence intensity ($u_{\rm RMS}/U$) strongly influences the characteristics of the flame front, where $u_{\rm RMS}$ and U are the root-mean-square of velocity fluctuations and the mean velocity in the reactants region, respectively. For relatively small values of the turbulence intensity, i.e., $u_{\rm RMS}/U \lesssim 0.06$, observations reported in Shanbhogue [9], Petersen and Emmons [10], and Kheirkhah and Gülder [8] indicate that the flame front corrugations are periodic and symmetric in the space domain. To the best knowledge of the authors, details associated with these characteristics are yet to be investigated in detail. Since the flame-holder utilized in the present investigation has a circular cross section, a brief review of isothermal flow development over circular cylinders are presented. Then, findings of past studies associated with the effect of heat release on the flow development are reviewed.

Several investigations have been performed in the past decades to study the development of isothermal flow over circular cylinders; see, for example, the review papers by Berger and Wille [11], Bearman [12], Choi *et al.* [13], and Williamson [14]. These investigations[11–14] show that

the flow development is strongly affected by the Reynolds number estimated based on the diameter of the cylinder (Re_d). For $Re_d \lesssim 5$, the flow is attached to the surface of the cylinder, and the corresponding flow regime is called the creeping flow [15]. For $5 \lesssim Re_d \lesssim 50$, the flow is composed of two steady recirculation zones behind the cylinder, and the pertaining flow regime is referred to as the laminar steady regime [14, 15]. Results provided in Zdravkovich [15] show that, for $50 \lesssim Re_d \lesssim 200$, which is known as the laminar vortex shedding regime [14], a global instability develops in the wake of the cylinder. This instability leads to periodic formation and shedding of vortical flow-structures in the wake of the circular cylinder, known as von Kármán vortex street. The vortex shedding frequency (f_{v}) can be obtained from the following equation[15, 16]:

$$St = \frac{f_{\mathrm{v}} d}{U}, \tag{1}$$

where St is referred to as the Strouhal number. For the laminar vortex shedding regime, the Strouhal number increases from approximately 0.12 to 0.19 by increasing the Reynolds number from about 50 to 200 [15, 16]. For $200 \lesssim Re_d \lesssim 400$, transition to turbulence occurs in the wake of the cylinder, and the corresponding regime is referred to as the wake transition regime [15]. In this regime, the Strouhal number (St) varies between approximately 0.19 and 0.21. For $400 \lesssim Re_d \lesssim 10^5$, transition to turbulence occurs in the shear layers developed on both sides of the cylinder[15, 17]; and the corresponding regime is referred to as the shear layer transition regime [14]. In this regime, the Strouhal number is approximately 0.21. For Reynolds numbers beyond 10^5, the transition to turbulence takes place in the boundary layers developed on both sides of the cylinder, and the corresponding regime is referred to as the boundary layer transition regime [18, 19]. The Strouhal number associated with the boundary layer transition regime varies between about 0.2 and 0.5 [15, 18, 19]. Further details associated with isothermal flow development over circular cylinders can be found in Zdravkovich[15].

Previous studies show that the combustion heat release influences the flow development over circular cylinders [20–26]. This influence can be elaborated using the vorticity transport equation [20], given by:

$$\frac{\mathrm{D}\overrightarrow{\omega}}{\mathrm{D}t} = (\overrightarrow{\omega}\cdot\overrightarrow{\nabla})\overrightarrow{V} + \nu\nabla^2\overrightarrow{\omega} + \frac{\overrightarrow{\nabla}\rho\times\overrightarrow{\nabla P}}{\rho^2} - \overrightarrow{\omega}(\overrightarrow{\nabla}\cdot\overrightarrow{V}). \tag{2}$$

In Eq. (2), $\overrightarrow{\omega}$, $\overrightarrow{V}$, ν, ρ, and P refer to vorticity vector, velocity vector, kinematic viscosity, fluid density, and pressure, respectively. The term on the left-hand-side (LHS) of Eq. (2) is the total derivative of the vorticity vector. The first term on the right-hand-side (RHS) is referred to as the vortex stretching and is related to the normal strain in the direction of the vorticity vector. This strain results in narrowing of the vortex tubes, and, as a result, increasing the vorticity values. The second term on the RHS of Eq. (2) is the viscous diffusion term. This term acts as a sink and decreases the vorticity values via the diffusion mechanism [21]. Since the fluid kinematic viscosity increases significantly in the products region, the viscous diffusion term is more pronounced in the products. Thus, the vorticity values decrease significantly across the flame front, from the reactants towards the products. The third term on the RHS of Eq. (2) is produced due to misalignment between the pressure and density gradients. This is a source term and is referred to as the baroclinic vortex generation term [20]. For unconfined flames, which is the case for the present study, the pressure change across the flame region is insignificant; and, as a result, the baroclinic vortex generation is negligible. The last term in the RHS of Eq. (2) is the fluid dilatation term. Due to the significant increase of the velocity through the flame, this term is relatively large.

Arguments provided in past investigations [20, 21, 27] indicate that, for unconfined flames, the combustion heat release can influence the vorticity equation via the viscous diffusion and the dilatation mechanisms, that are associated with the second and the last terms on the RHS of Eq. (2). Specifically, these mechanisms can affect the formation of the von Kármán vortex street. Results of past investigations associated with formation of the von Kármán vortex street under reacting

condition are controversial. Specifically, results presented in Erickson *et al.* [22] and Hertzberg *et al.* [24] show that the von Kármán vortex street exists in the wake of the flame-holder; however, results of Yamaguchi *et al.* [25] and Bill and Tarabanis [26] indicate that it is suppressed under reacting condition. Arguments provided in Shanbhogue *et al.* [21] show that either existence or suppression of the vortex street under reacting condition is strongly dependent on the burnt to unburnt gas temperature ratio ($T_\mathrm{b}/T_\mathrm{u}$). Specifically, Shanbhogue *et al.* [21] and Erickson *et al.* [22] show that strengths of the sink terms in Eq. (2), that are viscous diffusion and dilatation terms, are correlated with $T_\mathrm{b}/T_\mathrm{u}$. Their results [21, 22] show that, for $T_\mathrm{b}/T_\mathrm{u} \lesssim 2$, decreasing the burnt to unburnt gas temperature ratio decreases the strengths of the sink terms in Eq. (2); and, as a result, the von Kármán vortex street persists in the wake of the flame-holder. However, for large values of the burnt to unburnt gas temperature ratios ($T_\mathrm{b}/T_\mathrm{u} \gtrsim 2$), the viscous diffusion and dilatation mechanisms suppress the formation of the von Kármán vortex street.

Although past investigations [20–28] provide significant insight into vortex dynamics associated with turbulent premixed flames, connection between characteristics of the non-reacting flow over the flame-holder and those of the flame fronts are yet to be investigated. Specifically, this connection is studied utilizing the Proper Orthogonal Decomposition (POD) technique. Although application of this technique for investigating non-reacting flow has been utilized in numerous past studies, the authors believe that utilizing the POD analysis for investigating the flame surface characteristics is performed for the first time in this article.

2. Experimental Methodology

Details of the experimental setup utilized for producing V-shaped flames, the measurements techniques, and the experimental conditions tested are provided in this section.

2.1. Experimental Setup

The V-shaped flames were produced using the burner setup presented in Fig. 1(a). The burner is composed of an expansion section, a settling chamber, a contraction section, a nozzle, a flame-holder support, and a flame-holder. The expansion section has an expansion area ratio of about four. Close to the entrance of the expansion section, a baffle disk is placed in order to disperse the entering air-fuel mixture and the seeding flow, see Fig. 1(a). A settling chamber, equipped with five square-mesh screens, is installed after the expansion section for flow conditioning purposes. The settling chamber is followed by a contraction section with a contraction area ratio of approximately seven. After the contraction section, a nozzle with inner diameter (D) of 48.4 mm is placed. A circular flame-holder, made of stainless steel, is placed close to the exit of the nozzle, see Figs. 1(a) and 1(b). The flame-holder diameter (d) is 2 mm. Using the flame-holder support, the distance between the flame-holder centerline and the exit plane of the burner was fixed at 4 mm during all experiments.

The coordinate system utilized in the present investigation is Cartesian, as shown in Fig. 1(b). The origin of the coordinate system is located equidistant from both ends of the flame-holder, and 5 mm above the burner exit plane. The y-axis of the coordinate system is normal to the exit plane of the burner. The x-axis is normal to both y-axis and the flame-holder centerline. The z-axis is normal to both x and y axes and lies along the span of the flame-holder.

2.2. Measurement Techniques

Mie scattering and Particle Image Velocimertry (PIV) techniques were utilized in the present study. The former was used to investigate characteristics of non-reacting flow, and the latter was utilized to study those of the flame front contour. Details pertaining to these techniques are presented below.

Mie Scattering

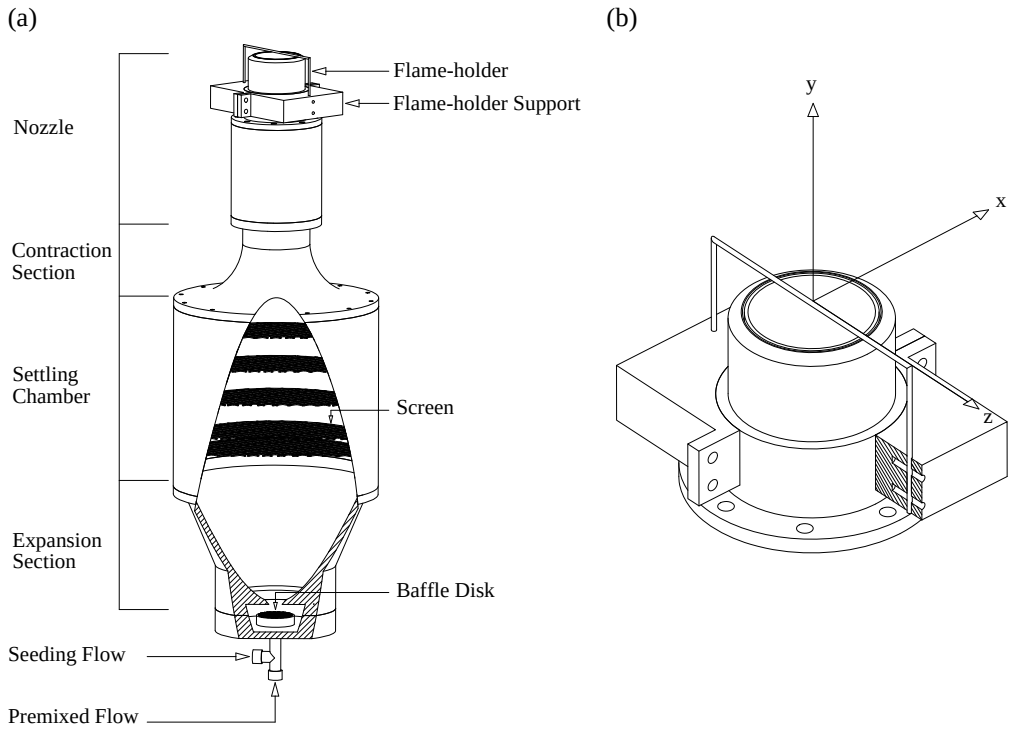

Fig. 1. (a) Burner setup and (b) flame-holder and flame-holder support details.

The Mie scattering technique was utilized to obtain the flame front contour. As defined by Eckbreth [29], the Mie scattering is elastic scattering of light, with wave length λ, from particles with average size d_{p}, when $d_{\mathrm{p}} \gtrsim \lambda$. The Mie scattering technique is widely used in the past experimental investigations pertaining to V-shaped flames, see, for example, [30–37]. An underlying assumption in application of the Mie scattering technique is that combustion occurs inside a relatively thin layer [35–37]. This assumption is referred to as the flamelet assumption [38]. Implication of the flamelet assumption is that if the reactants are seeded with particles which evaporate at the flame front, the light intensities scattered from the particles inside the reactants region will be significantly larger than those inside the products region. This marked difference in the light intensities is utilized for detection of the flame front [34–37]. A Laskin-nozzle type nebulizer, previously utilized in the studies of Smallwood *et al.* [39], Gülder [40], and Kheirkhah and Gülder [37] was used for seeding purposes in the Mie scattering experiments. The olive oil droplets, which have been previously assessed to

be proper for Mie scattering experiments in the past investigations [37, 41], were utilized in the present study.

The hardware associated with the Mie scattering technique consists of a CCD camera and a Nd:YAG pulsed laser. The camera has a resolution of 2048 pixels by 2048 pixels. The camera head is equipped with a macro Sigma lens, which has a focal length (f) of 105 mm. During the experiments, the lens aperture size was fixed at $f/8$. In order to avoid influence of flame chemiluminescence in acquired images, the lens was equipped with a 532 nm band-pass filter. For all the experiments, imaging field of view was 60 mm $\times$ 60 mm.

The flow field was illuminated by a laser sheet formed from a 6.5 mm diameter beam, which has a wavelength of 532 nm, a beam energy of about 120 mJ per pulse, and a pulse duration of about 4 ns. At the plane of $z/d = 0$, where all the experiments were performed, the laser sheet thickness was measured to be approximately 150 ± 50 μm. The laser operated at a frequency of 5 Hz and the Mie scattering images were simultaneously acquired by the CCD camera. For statistical analysis purposes, 1000 images were acquired for each experimental condition tested.

The recorded images were binarized using a threshold-based technique. The binarization process is usually accompanied by digitization noise [42]. In order to reduce the noise, a median-finding-based algorithm was utilized to filter the binarized images. The filter size was selected to be equal to the inner cutoff scale [42] (ϵ_{i}). The value of the inner cutoff scale was estimated from: $\epsilon_{\mathrm{i}} = 7\delta_{\mathrm{L}} Ka^{-1/2}$ proposed by Roberts *et al.* [43], where δ_{L} and Ka are the laminar flame thickness and the Karlovitz number, respectively. Depending on the experimental condition tested, value of ϵ_{i} was varied between 1.3 mm and 2.5 mm. After filtering the binarized images, the contour algorithm in MATLAB was used to obtain the flame front.

Particle Image Velocimetry

The Particle Image Velocitmetry (PIV) technique was utilized to measure the velocity field

for non-reacting flow condition. The PIV experiments were performed for estimating the velocity characteristics pertaining to the background flow field as well as the flow field associated with the wake of the flame-holder. The former was used to estimate the background turbulence intensity as well as the integral length scale, and the latter was utilized to study the dominant flow-structures. The PIV hardware is identical to that utilized for the Mie scattering experiments. All the PIV experiments were performed at the plane of $z/d = 0$. For each experimental condition tested, 1000 PIV images were acquired at a frequency of 5 Hz. For velocity data analysis, the interrogation window size was selected to be 16 pixels by 16 pixels, with zero overlap between the windows. This results in the velocity data matrices with a size of 128 $\times$ 128. For each experimental condition, the separation time between the laser pulses, was selected such that the average distance traced by the seeding particles in each interrogation window was approximately 25% of the size of each interrogation window. This was performed in order to avoid particles loss between consecutive images. Olive oil droplets were used for seeding in the PIV experiments. These droplets were previously assessed [37] to be proper for the flow seeding.

2.3. Experimental Conditions

The tested experimental conditions are tabulated in Table I. Methane grade 2, i.e., methane with 99% chemical purity, was used as the fuel in the experiments. Three mean bulk flow velocities of $U = 4.0$, 6.2, and 8.3 m/s were examined. The mean bulk flow velocity was estimated from $U = 4\dot{m}/(\pi\rho_{\mathrm{u}}D^2)$, where $\dot{m}$ and ρ_{u} are mass flow rate and density of the fuel-air mixture, respectively. The Reynolds number pertaining to the mean bulk flow velocities were estimated based on the diameter of the flame-holder ($Re_d = Ud/\nu$), with $\nu = 1.57\times10^{-5}\mathrm{m}^2/\mathrm{s}$ being the reactants kinematic viscosity at standard temperature and pressure conditions. For each mean bulk flow velocity, two fuel-air equivalence ratios of $\phi = 0.6$ and 0.7 were tested in the experiments. In Table I, the unstretched laminar flame speed (S_{L0}) was extracted from Yu *et al.* [44]. The laminar flame thickness

Table 1. Tested experimental conditions.

	Symbol	U(m/s)	Re_d	ϕ	S_{L0}(m/s)	δ_{L}(mm)	u_{RMS}/U	Λ(mm)
Flame A	○	4.0	510	0.6	0.13	0.17	0.02	2.6
Flame B	□	4.0	510	0.7	0.20	0.11	0.02	2.6
Flame C	◁	6.2	790	0.6	0.13	0.17	0.02	2.5
Flame D	▷	6.2	790	0.7	0.20	0.11	0.02	2.5
Flame E	◇	8.3	1057	0.6	0.13	0.17	0.02	2.4
Flame F	×	8.3	1057	0.7	0.20	0.11	0.02	2.4

was estimated from: $\delta_{\mathrm{L}} = \mathcal{D}/S_{\mathrm{L0}}$, where $\mathcal{D} = \nu/(PrLe)$. The Lewis (Le) and the Prandtl numbers (Pr) are estimated for the reactants mixture at standard temperature and pressure conditions; and are approximately unity and 0.71, respectively. The turbulence intensity (u_{RMS}/U) was estimated for the background flow field, with u_{RMS} being measured at $x/d = 0$, $y/d = -1$, and $z/d = 0$. For each experimental condition, the integral length scale was estimated using the streamwise velocity autocorrelation [45] calculated along the vertical axis, with details of analysis provided in Kheirkhah and Gülder [8]. All the experimental conditions are overlaid on the premixed combustion regime diagram presented in Fig. 2. The results show that the experimental conditions pertain to the wrinkled as well as corrugated flames.

3. Results

A representative Mie scattering image associated with Flame E condition is presented in Fig. 3(a). Overlaid on the figure is the flame front contour obtained from the Mie scattering technique

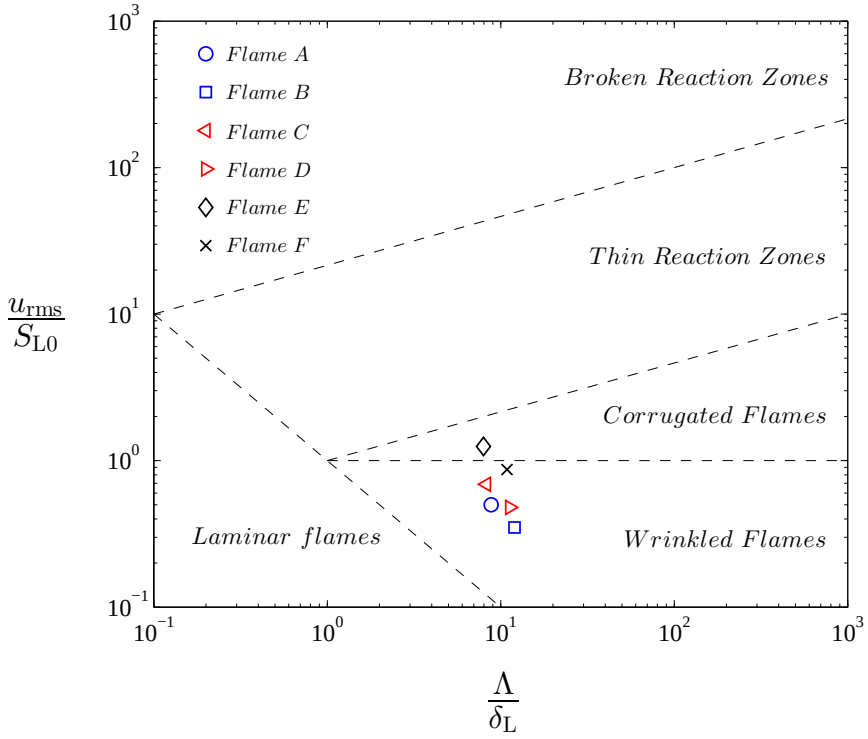

Fig. 2. Experimental conditions overlaid on the premixed combustion regime diagram [1].

with corresponding details provided in the previous section. Insets of Fig. 3(a) pertaining to the left and right wings of the flame fronts are presented in Figs. 3(b) and 3(c), respectively. Results in the figures show that: (a) the flame front corrugations are symmetric with respect to the vertical axis, and (b) the corrugations feature a nearly periodic pattern. In order to investigate these characteristics, the results are grouped in three subsections. First, details associated with non-reacting flow over the circular cylinder is investigated. Then, in the second and the third subsections, underlying details pertaining to symmetry and periodicity in flame front corrugations are studied, respectively.

3.1. Non-reacting flow characteristics

For all experimental conditions tested, the POD technique, with details provided in [46–48] was utilized for analysis of the velocity data pertaining to non-reacting flow over the circular cylinder. Specifically, the following matrix was constructed:

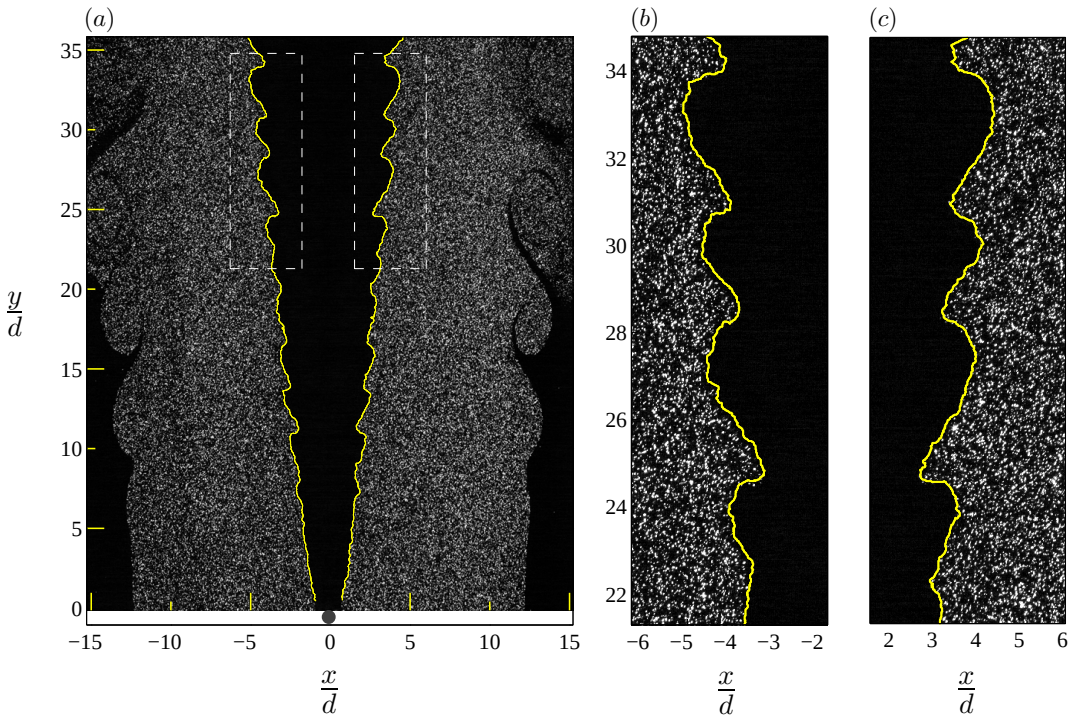

Fig. 3. (a) Mie scattering image associated with Flame E condition. (b) and (c) are insets of (a) pertaining to the left and right wings of the flame fronts, respectively.

$$\boldsymbol{P} = [\boldsymbol{p}^1\ \boldsymbol{p}^2\ \boldsymbol{p}^3\ \ldots\ \boldsymbol{p}^N] = \begin{bmatrix} u_1'^1 & u_1'^2 & u_1'^3 & \ldots & u_1'^N \\ u_2'^1 & u_2'^2 & u_2'^3 & \ldots & u_2'^N \\ u_3'^1 & u_3'^2 & u_3'^3 & \ldots & u_3'^N \\ \vdots & \vdots & \vdots & \vdots & \vdots \\ u_K'^1 & u_K'^2 & u_K'^3 & \ldots & u_K'^N \\ v_1'^1 & v_1'^2 & v_1'^3 & \ldots & v_1'^N \\ v_2'^1 & v_2'^2 & v_2'^3 & \ldots & v_2'^N \\ v_3'^1 & v_3'^2 & v_3'^3 & \ldots & v_3'^N \\ \vdots & \vdots & \vdots & \vdots & \vdots \\ v_K'^1 & v_K'^2 & v_K'^3 & \ldots & v_K'^N \end{bmatrix}, \tag{3}$$

where $\boldsymbol{p}^i = [u_1'^i \; u_2'^i \; u_3'^i \; \ldots \; u_K'^i \; v_1'^i \; v_2'^i \; v_3'^i \ldots \; v_K'^i]^{\mathrm{T}}$, with u' and v' being the fluctuations of the streamwise and transverse velocity data. Specifically, $u' = u - \overline{u}$ and $v' = v - \overline{v}$, with $\overline{u}$ and $\overline{v}$ being the mean streamwise and transverse velocities, respectively. Each column of $\boldsymbol{P}$ corresponds to velocity fluctuations associated with a given PIV image. Thus, the number of columns in $\boldsymbol{P}$ pertains to the number of PIV images acquired, i.e., $N = 1000$. In Eq. (3), the subscript K is the total number of streamwise or transverse velocity data associated with a given PIV image, meaning that $K = 128 \times 128 = 16384$. Using the matrix of velocity fluctuations, the autocovariance matrix ($\boldsymbol{Q} = \boldsymbol{P}^{\mathrm{T}}\boldsymbol{P}$) was estimated. Then, eigenvalues and eigenvectors of $\boldsymbol{Q}$ were obtained by solving the following equation:

$$\boldsymbol{Q}\boldsymbol{H}^i = \gamma^i \boldsymbol{H}^i, \tag{4}$$

where γ^i and $\boldsymbol{H}^i$ are the i^{th} eigenvalue and eigenvector, respectively. The eigenvalues were estimated and arranged in a descending order, meaning that γ^1 and γ^N correspond to the largest and the smallest eigenvalues, respectively. For all experimental conditions tested, the eigenvalues are presented in Fig. 4(a). Note that, since the analysis is performed for non-reacting flow condition, the results are only presented for experimental conditions of A, C, and E. Results pertaining to experimental conditions of B, D, and F are identical to those pertaining to A, C, and E, respectively. As can be seen from the results in Fig. 4(a), for all experimental conditions tested, the first and the second POD modes are relatively large; however, increasing the mode number substantially decreases γ. Since γ^1 and γ^2 are relatively large, the first and the second modes are commonly considered as the most energetic modes in several investigations associated with non-reacting flow over circular cylinders [49, 50]. In this study, the methodology presented in Epps and Techet [51] was utilized to obtain the most energetic POD modes. Using uncertainty arguments, Epps and Techet [51] estimated a threshold eigenvalue (γ_{t}) given by the following formulation:

$$\gamma_t = KN\epsilon^2, \tag{5}$$

where ϵ is the error associated with estimation of the velocity data. Assuming negligible bias error, it can be shown that ϵ approximately equals the ratio of the RMS velocity fluctuations to the square root of the number of PIV images. Our analysis shows that the RMS streamwise (u') and transverse (v') velocity fluctuations are maximized in the near wake of the cylinder, with the values of v' being larger. Thus, the maximum value of v' was utilized for estimation of the threshold eigenvalue. The results show that γ_t is approximately equal to 3.3×10^4 m^2/s^2, 7.4×10^4 m^2/s^2, and 9.7×10^4 m^2/s^2 for $Re_d = 510$, 790, and 1057, respectively. Results presented in Fig. 4(a) show that eigenvalues associated with modes 1-7, 1-6, and 1-8 are larger than the threshold eigenvalue associated with experimental conditions of A, C, and E, respectively. The corresponding data points are highlighted by the data symbols in Fig. 4(a). The results in the figure suggest that relatively small number of POD modes, approximately first 6 modes, are not contaminated by the velocity data error. Thus, these modes can be utilized for the POD analysis of the velocity data.

The normalized cumulative mode energies ($\sum_{i=1}^{i=n} \gamma^i / \sum_{i=1}^{i=N} \gamma^i$) associated with the results in Fig. 4(a) are presented in Fig. 4(b). The results in Fig. 4(b) show that, for $n \geq 4$, increasing the Reynolds number, decreases the cumulative mode energy. This is associated with pronounced distribution of the turbulent kinetic energy at large mode numbers with increase of the Reynolds number. Specifically, it was previously presented that the background turbulence intensity is approximately constant ($u_{\mathrm{RMS}}/U \approx 0.02$) for all experimental conditions tested, see Table I. Thus, increasing the Reynolds number, which is synonymous with increasing U, increases the velocity fluctuations associated with the background turbulence (u_{RMS}). On one hand, since the turbulent flow kinetic energy is directly related to u_{RMS}, increasing Re_d increases the kinetic energy of the background turbulent flow. On the other hand, the kinetic energy of the background turbulent flow

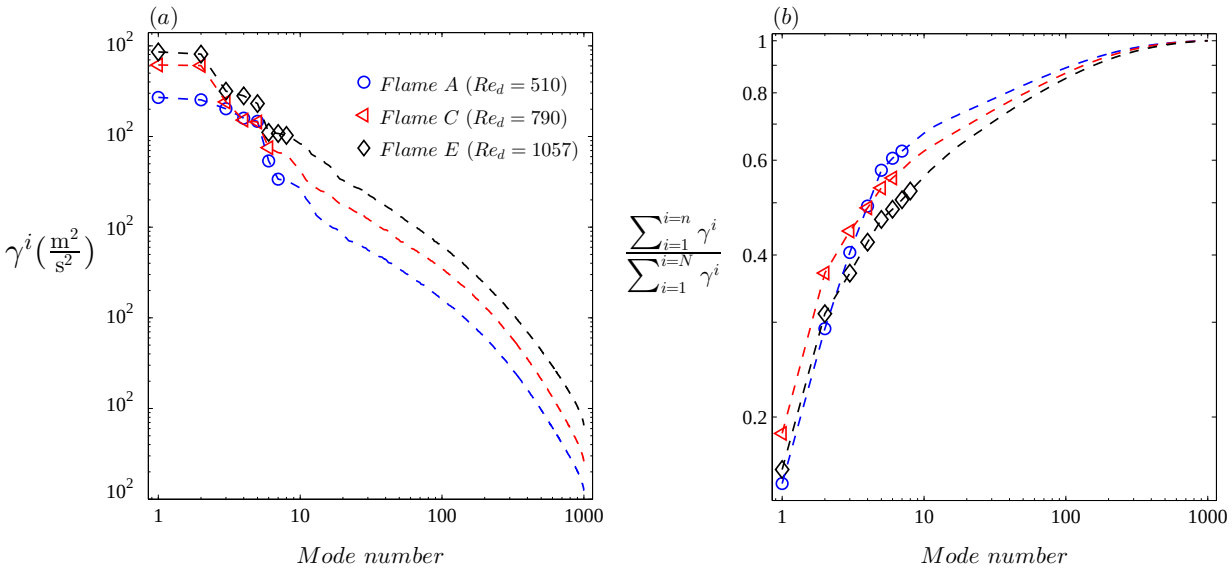

Fig. 4. (a) Eigenvalues of the velocity data. (b) Cumulative mode energy associated with the results presented in (a).

is distributed amongst large POD modes. Therefore, increasing the Reynolds number distributes the kinetic energy in relatively larger mode numbers. This results in decrease of the cumulative mode energy with increase of the Reynolds number.

Using the eigenvectors estimated from Eq. (4), the normalized POD mode shapes ($\boldsymbol{\theta}^i$) associated with the velocity data were obtained using the following formulation:

$$\boldsymbol{\theta}^i = \frac{\sum_{n=1}^{n=N} h_n^i \boldsymbol{p}^n}{|\sum_{n=1}^{n=N} h_n^i \boldsymbol{p}^n|}, \tag{6}$$

where h_n^i is the n^{th} component of the i^{th} eigenvector. Also, the symbol $(|*|)$ represents the second norm of a matrix. The POD mode shapes estimated from Eq. (6) are matrices with the size of $2K \times 1$. In order to investigate characteristics of the dominant flow-structures, these mode shapes were cast into two dimensional matrices. Specifically, for the i^{th} mode shape, the first and the second K components of $\boldsymbol{\theta}^i$, that are $\boldsymbol{\theta}^i(1:K)$ and $\boldsymbol{\theta}^i(K+1:2K)$, were cast into two 128×128 matrices pertaining to the i^{th} POD mode of the streamwise and transverse velocity data, respectively. It

was previously argued that, for the experimental conditions of the present study, mainly modes 1-6 are significant, meaning that these modes are not influenced by the velocity data error. For the analysis presented here and for simplicity of the arguments, only the first ($\boldsymbol{\theta}^1$) and the second ($\boldsymbol{\theta}^2$) POD mode shapes are presented and discussed. Specifically, the first and the second POD mode shapes associated with the streamwise velocity data are presented in Figs. 5(a) and 5(b), respectively. Similarly, the first and the second POD mode shapes pertaining to the transverse velocity data are shown in Figs. 5(c) and 5(d), respectively. In Fig. 5, the negative contours are specified by the overlaid solid curves. The results in Fig. 5 show that the POD mode shapes feature patches of negative and positive values which repeat in the space domain. This is similar to the results presented in past investigations pertaining to flow over circular cylinders, see, for example, Sengupta *et al.* [52]. Representative variations of the mode shape values associated with Figs. 5(a), 5(b), 5(c), and 5(d) are presented in Figs. 6(a), 6(b), 6(c), and 6(d), respectively. The results in Figs. 6(a) and 6(b) are associated with $x/d = 1.5$ and those in Figs. 6(c) and 6(d) pertain to $x/d = 0$. Using the results presented in Fig. 6, the vertical distance between two neighbouring local maximums were estimated. This distance normalized by the flame-holder diameter is referred to as l^* and is highlighted in Fig. 6(a). Sensitivity analysis shows that l^* estimated based on the vertical distance between two neighbouring local maximums and two local minimums are identical. Also, the results show that l^* is independent of the first and the second POD modes pertaining to either of the streamwise or transverse velocity data, and is approximately 4.2 for all experimental conditions tested. This normalized length scale is considered as the length scale of dominant instability in the wake of the circular cylinder.

It is of interest to investigate the reason associated with the value of l^* being independent of the experimental conditions tested. As it is demonstrated in the following as well as several past investigations pertaining to flow over circular cylinders [14, 15], the corresponding wake is dominated

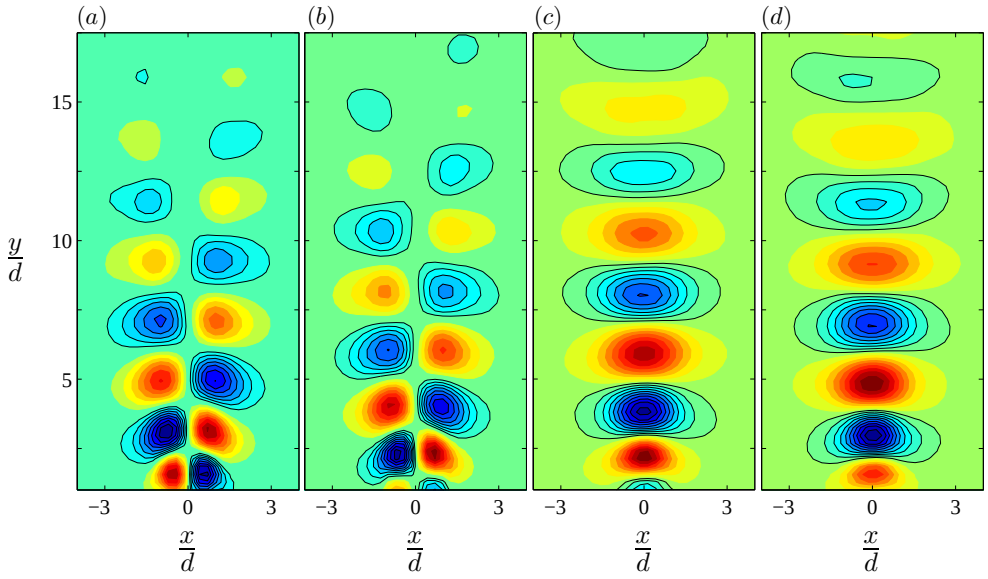

Fig. 5. (a) and (b) correspond to the first and the second POD modes of the streamwise velocity data, respectively. (c) and (d) pertain to the first and the second POD modes of the transverse velocity data, respectively. The results are associated with Flame E condition.

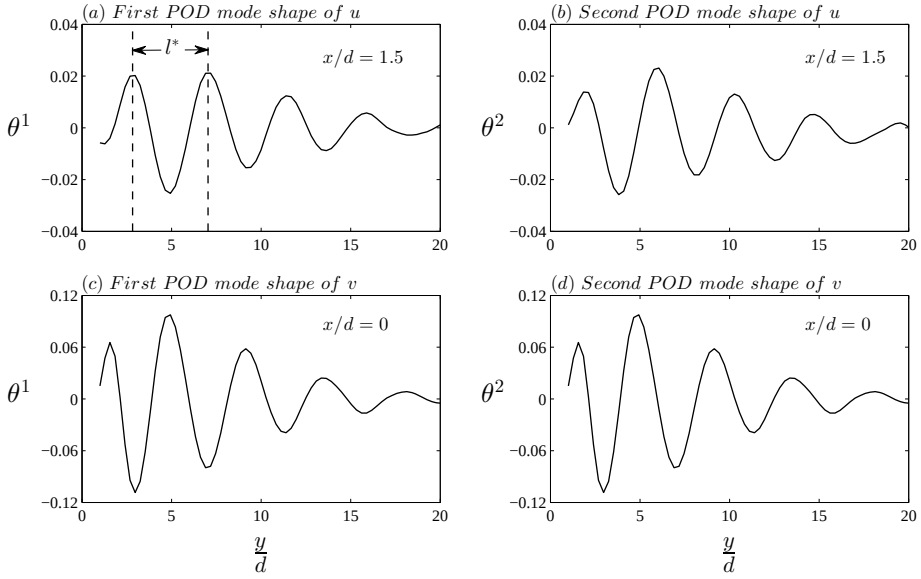

Fig. 6. (a) and (b) are variations of the first and the the second POD mode shapes associated with the streamwise velocity data, respectively. (c) and (d) are variations of the POD mode shapes pertaining to the transverse velocity data, respectively. Results in (a, b) as well as (c, d) are associated with $x/d = 1.5$ and 0, respectively. All variations are extracted from corresponding results presented in Fig. 5.

by the vortex shedding phenomenon for Reynolds numbers similar to those of the present study. Assuming that l is the distance traveled by a given flow-structure in one time period of vortex shedding, it can be shown that $l = U/f_{\mathrm{v}}$, with f_{v} being the vortex shedding frequency and is given by Eq. (1). This argument suggests that the Strouhal number, see Eq. (1), and l^* are related by:

$$St \approx \frac{1}{l^*}. \tag{7}$$

Since the Strouhal number is approximately 0.21 for the Reynold numbers investigated in the present study, see, for example, Zdravkovich [15], l^* requires to be constant, which is in agreement with the results presented earlier. Utilizing the value of Strouhal number along with Eq. (7), it can be shown that l^* is approximately 4.5, which is in reasonable agreement with the the results presented in Figs. 5 and 6.

Equation (7) was derived assuming that l is the vertical distance between two neighbouring coherent flow-structures. In order to assess validity of this assumption, the velocity data was reconstructed using the POD modes. This was performed using:

$$\begin{bmatrix} \boldsymbol{u}_r^i \\ \\ \boldsymbol{v}_r^i \end{bmatrix} \approx \begin{bmatrix} \overline{\boldsymbol{u}} \\ \\ \overline{\boldsymbol{v}} \end{bmatrix} + \boldsymbol{\eta}\boldsymbol{\eta}^{\mathrm{T}}\boldsymbol{p}^i, \tag{8}$$

where $\boldsymbol{\eta}$ is associated with the most dominant modes and is given by $\boldsymbol{\eta} = [\boldsymbol{\theta}^1\ \boldsymbol{\theta}^2\ \boldsymbol{\theta}^3 \ldots \boldsymbol{\theta}^6]$. In Eq. (8), the superscript i pertains to the data associated with the i^{th} PIV image. In the equation, $\overline{\boldsymbol{u}}$ and $\overline{\boldsymbol{v}}$ are the mean streamwise and transverse velocity data and are given by $\overline{\boldsymbol{u}} = [\overline{u_1}\ \overline{u_2}\ \overline{u_3}\ \ldots\ \overline{u_K}]^{\mathrm{T}}$ and $\overline{\boldsymbol{v}} = [\overline{v_1}\ \overline{v_2}\ \overline{v_3}\ \ldots\ \overline{v_K}]^{\mathrm{T}}$, respectively. Equation (8) can be written in terms of temporal POD coefficients and the dominant POD mode shapes. Specifically, the reconstructed streamwise and transverse velocity data can be given by:

$$\begin{bmatrix} \boldsymbol{u}_r^i \\ \boldsymbol{v}_r^i \end{bmatrix} \approx \begin{bmatrix} \overline{\boldsymbol{u}} \\ \overline{\boldsymbol{v}} \end{bmatrix} + \sum_{j=1}^{j=6} a_j^i \boldsymbol{\theta}^j, \tag{9}$$

where a_j^i is referred to as the j^{th} temporal coefficient for reconstruction of the velocity data associated with the i^{th} PIV image. Figure 7(a) shows a representative vorticity ($\omega_z = \partial u/\partial x - \partial v/\partial y$) contour associated with Flame E condition. The negative vorticity contours are highlighted by solid curves for clarity purposes. The results demonstrate formation of the von Kármán vortex street, which is a characteristic of flow over circular cylinders for Reynolds numbers corresponding to those of the present study. In order to estimate distance between two neighbouring coherent flow-structures, variations of vorticity along several vertical distances were considered, with representative ones pertaining to $x/d = -0.7$ and 0.7 presented in Fig. 7(b). The results in Fig. 7(b) show that the normalized distance between two neighboring vortices is equal to approximately 4.2. This is identical to the normalized distance previously presented in Fig. 6(a). This similarity validates the assumption that the separation distance between two neigbouring coherent flow-structures in the streamwise direction is approximately equal to l.

The vorticity contours presented in Fig. 7(a) demonstrate formation of the von Kármán vortex street. In addition to the vorticity contours, correlation between the first (a^1) and the second (a^2) temporal coefficients were utilized to investigate the vortex shedding phenomenon. Specifically, past investigations, see, for example, Ruiz *et al.* [53], show that variation of the normalized first (a_j^1) and second (a_j^2) temporal coefficients associated with the velocity data nearly follow a unity radius circle centered at the origin. For the experimental condition associated with the results presented in Fig. 7(a), the normalized temporal coefficients were estimated and the results are presented in Fig. 7(c). As can be seen from the results in Fig. 7(c), the normalized coefficients nearly follow a unity radius circle centered at the origin. This is in agreement with past investigations associated

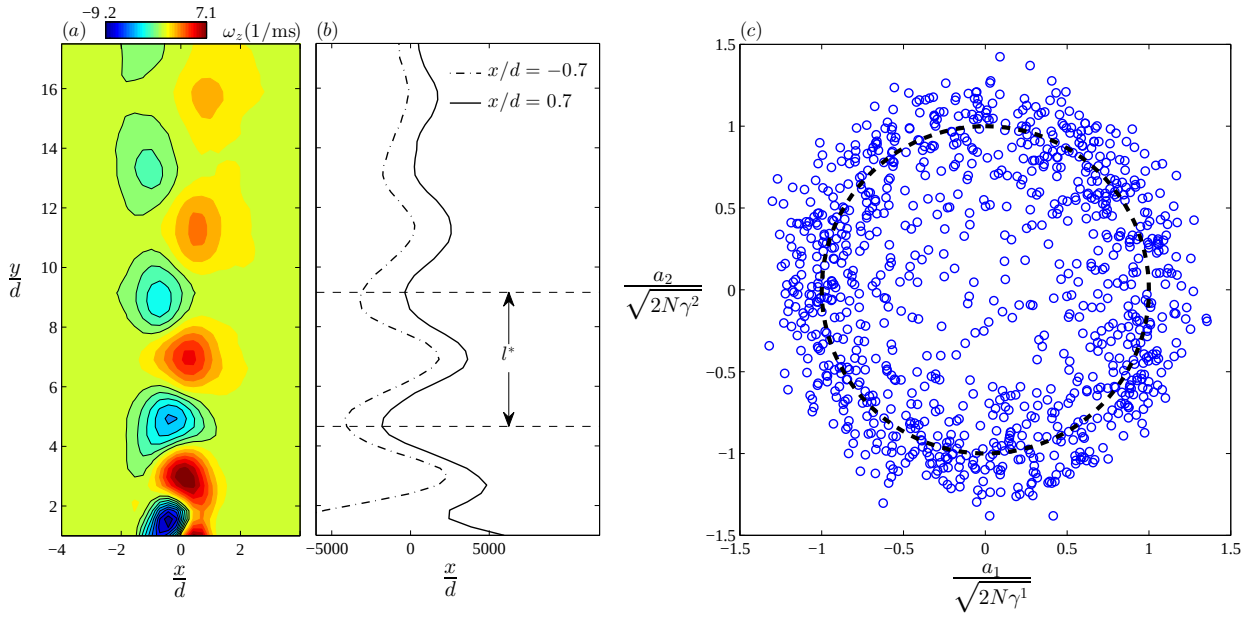

Fig. 7. (a) Representative vorticity contours estimated using the velocity data reconstructed from modes 1-6. (b) Variation of the vorticity presented in (a) along $x/d = -0.7$ and 0.7. (c) Variation of the normalized second POD coefficient versus the normalized first POD coefficient. The results pertain to Flame E condition presented in Table I.

with flow over bluff bodies [53–55]. Further details pertaining to this characteristic of the first and the second normalized temporal coefficients are discussed later in the manuscript.

3.2. Symmetry of the flame front corrugations

Results presented in Fig. 3 showed that the right and the left wings of the flame fronts are nearly symmetric with respect to the vertical axis. In order to investigate this characteristic of the flame fronts, variation of the flame front position along the vertical axis, $x(y)$, was utilized. The flame front position is the distance between a given point on the flame front contour and the vertical axis (y). The analyses presented in this subsection pertain to mean and RMS of the flame front position as well as the phase difference between the flame front positions associated with the right and the left wings of the flame contours. Representative flame front position signals, extracted from Mie scattering images, are shown in Fig. 8(a). The results in the figure pertain to those previously

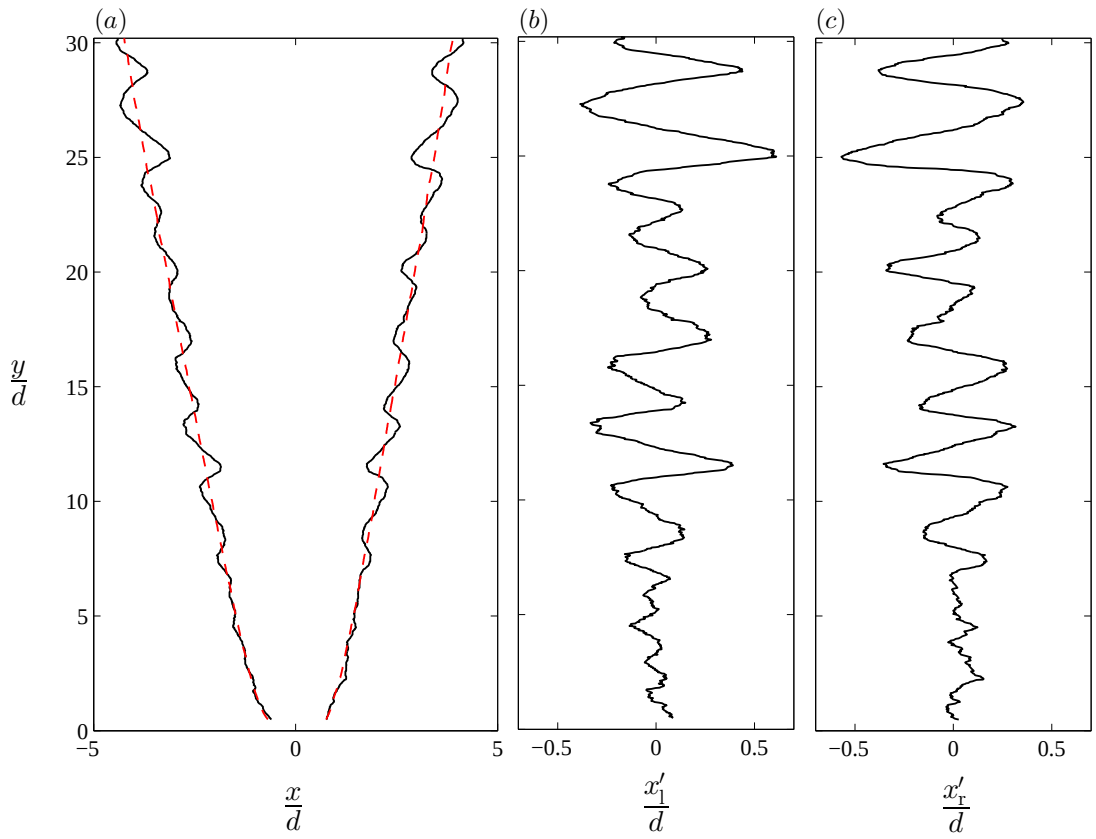

Fig. 8. (a) instantaneous flame front position associated with the results presented in in Fig. 3(a). The red dashed line pertains to the mean flame front position. (b) and (c) are fluctuations of the left and right flame front position along the vertical axis, respectively.

presented in Fig. 3(a). Mean flame front positions pertaining to both wings of the flame front are presented by the red dashed curves in Fig. 8(a). Also, fluctuations of the left (x'_l) and right (x'_r) wings of the flame fronts are presented in Figs. 8(b) and 8(c), respectively. For the results presented in the rest of the manuscript, signal similar to those shown in Fig. 8 were utilized for the analyses.

Mean and RMS of the flame flame position were estimated for all tested experimental conditions, and the corresponding results are shown in Figs. 9(a-c) and 9(d-f), respectively. In the figures, the first, the second, and the third columns pertain to mean bulk flow velocities of 4.0, 6.2, and 8.3 m/s, respectively. The uncertainty associated with the results are accommodated by the size of the data symbols. The results in the figure show that increasing the fuel-air equivalence ratio increases

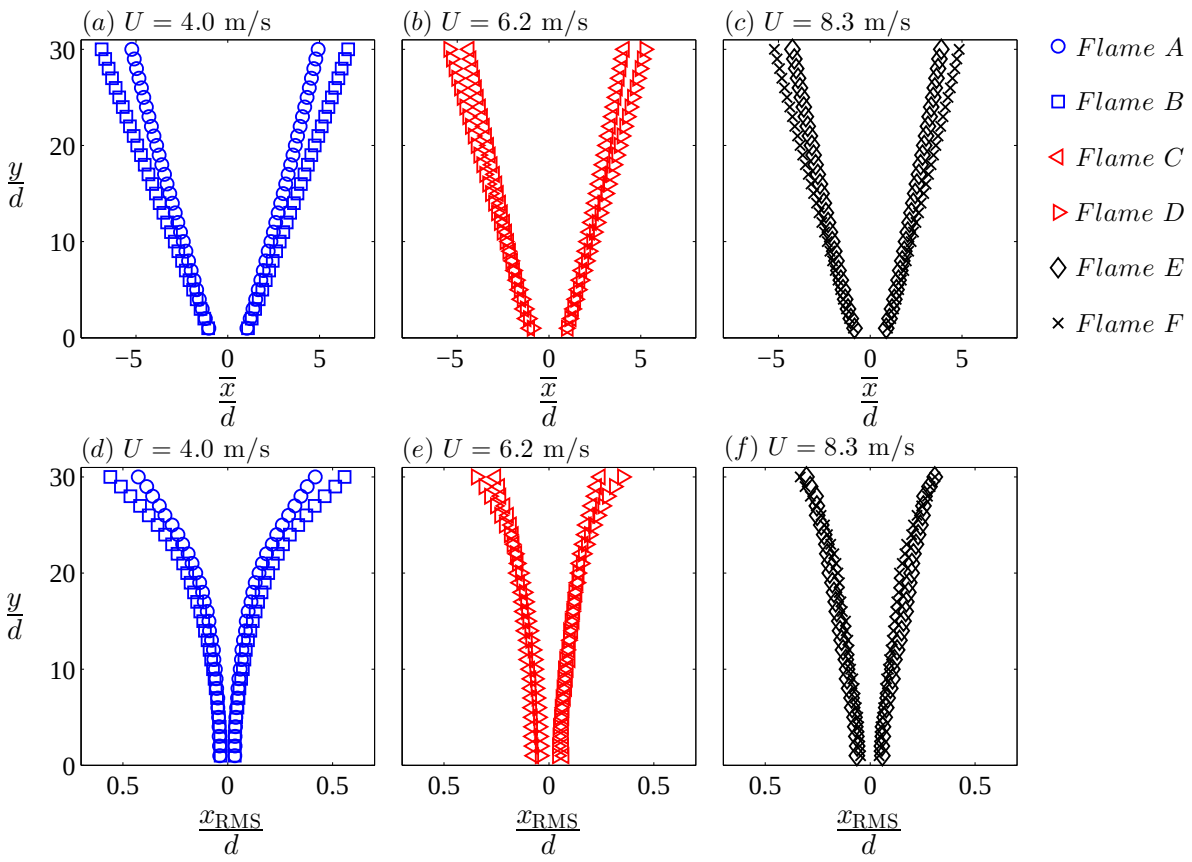

Fig. 9. (a-c) and (d-f) pertain to mean and RMS of the flame front position, respectively. The first, the second, and the third columns pertain to mean bulk flow velocities of 4.0, 6.2, and 8.3 m/s, respectively.

both $\overline{x}$ and x_{RMS}, with this influence becoming less pronounced with increasing the mean bulk flow velocity. This is a characteristic of lean premixed V-shaped flames and is investigated in detail in past investigations, see, for example, Goix *et al.* [7] and Kheirkhah and Gülder [37].

The results presented in Fig. 9 show that statistics of $x(y)$ is symmetric with respect to the vertical axis; however, this does not necessitates symmetry of the flame fronts. In order to assess this, phase difference ($\Delta\alpha$) between the right and the left wings of the flame front position were estimated, using the Hilbert transform technique. The phase of the flame front position (α) is equal to the phase of the complex function $r(y)$ given by:

$$r(y) = x'(y) - H[x'(y)]I, \tag{10}$$

where $I = \sqrt{-1}$, and $x'(y)$ is the fluctuations of the flame front position along the vertical axis, i.e., $x'(y) = x(y) - \overline{x}(y)$. Representative variation of $x'(y)$ associated with the right and the left wings of the flame front position were previously presented in Figs. 8(b) and 8(c), respectively. In Eq. (9), $H[x'(y)]$ is the Hilbert transform of the flame front position, and is given by:

$$H[x'(y)] = \frac{-1}{\pi y} * x'(y), \tag{11}$$

where the symbol $*$ is the convolution product. For further details associated with the Hilbert transform technique refer to Bracewell [56].

The phase of the right ($\alpha_{\rm r}$) and the left ($\alpha_{\rm l}$) wings of the flame front were estimated using Eqs. (10 and 11). Variations of the phase angles associated with the right and the left wings of the flame front are presented in Fig. 10(a). The corresponding phase difference ($\Delta\alpha = \alpha_{\rm r} - \alpha_{\rm l}$) is shown in Figs. 10(b). The results in Fig. 10(a) pertain to the flame front fluctuations presented in Figs. 8(b) and 8(c). The results in Fig. 10(a) show that variation of the phase angle along the vertical distance from the flame-holder features a sawtooth shape variation, which is more pronounced at relatively large values of y/d. This characteristic suggests that the flame front corrugations are nearly periodic in the space domain, with further details presented in the next subsection. The results in Fig. 10 show that, for relatively small vertical distances from the flame-holder ($y/d \lesssim 8$), $\alpha_{\rm r}$ and $\alpha_{\rm l}$ differ significantly; and, as a result, the phase difference is scattered. However, for relatively large vertical distances from the flame-holder $\alpha_{\rm r}$ and $\alpha_{\rm l}$ nearly collapse. Thus, the phase difference is relatively negligible for $y/d \gtrsim 8$, except at $y/d \approx 22$. In fact, for this normalized vertical distance, results in Fig. 10(b) show that $\alpha_{\rm r} - \alpha_{\rm l}$ is not negligible. The relatively large values of the phase difference at $y/d \approx 22$ is due to asymmetry of the flame fronts. In fact, results previously presented in Figs. 3(b) and 3(c) show that the flame fronts are nearly asymmetric at $y/d \approx 22$.

It is of interest to investigate the underlying reason associated with the symmetry in corrugations

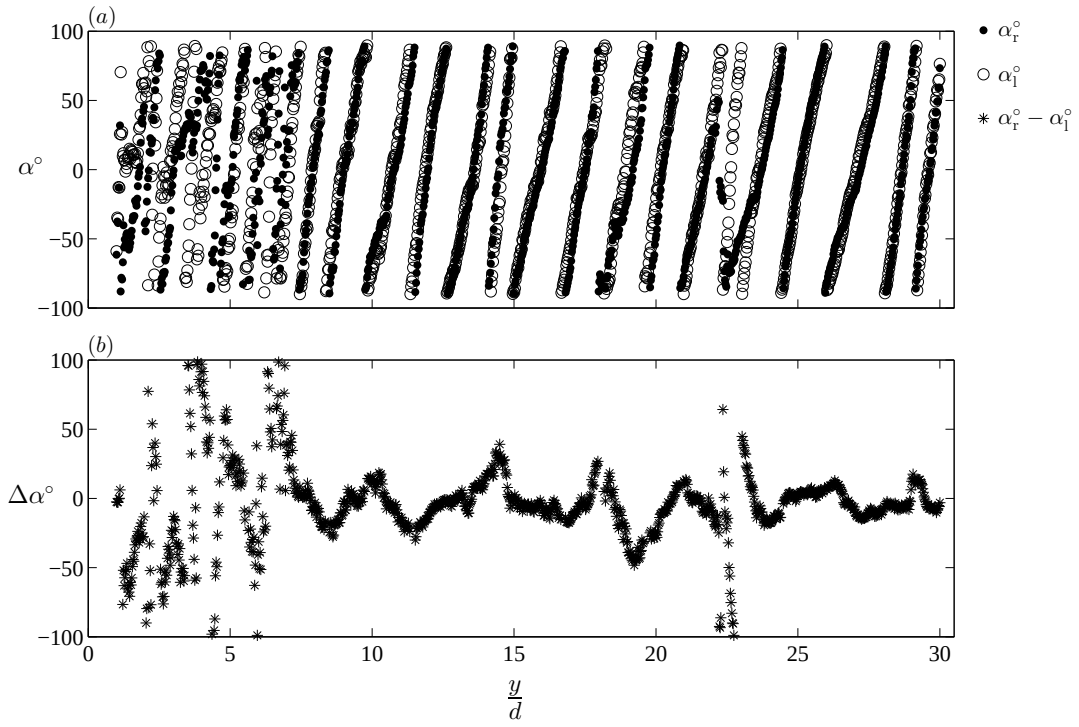

Fig. 10. (a) Instantaneous phase angles associated with the right (α_r) and the left (α_l) wings of the flame front presented in Fig. 3(a). (b) the phase difference pertaining to the results presented in (a).

of the flame surfaces. Past experimental investigations, e.g., Shanbhogue *et al.* [9, 57], show that, for the conditions pertaining to relatively small values of background turbulence intensity which pertain to the experimental conditions tested in the present study, the large eddies are surrounded by flame fronts. For this reason, the symmetric flame fronts observed in the present study are associated with symmetrically-positioned vortices in the domain of investigation. Figure 11 presents schematic of two symmetrically-positioned vortices surrounded by flame surfaces which are highlighted by solid black curves. Due to flow and flame front geometries, these vortices require to be counter-rotating. This means that vorticity variation (ω_z) features an odd function at a given vertical distance, with schematic variation presented in Fig. 11(b). In order to prove that the vorticity is an odd function for a given vertical distance, the vorticity transport formulation, Eq. (2), was utilized. Specifically, it was assumed that the flow field is two dimensional; and the vortex stretching as well as baroclinic

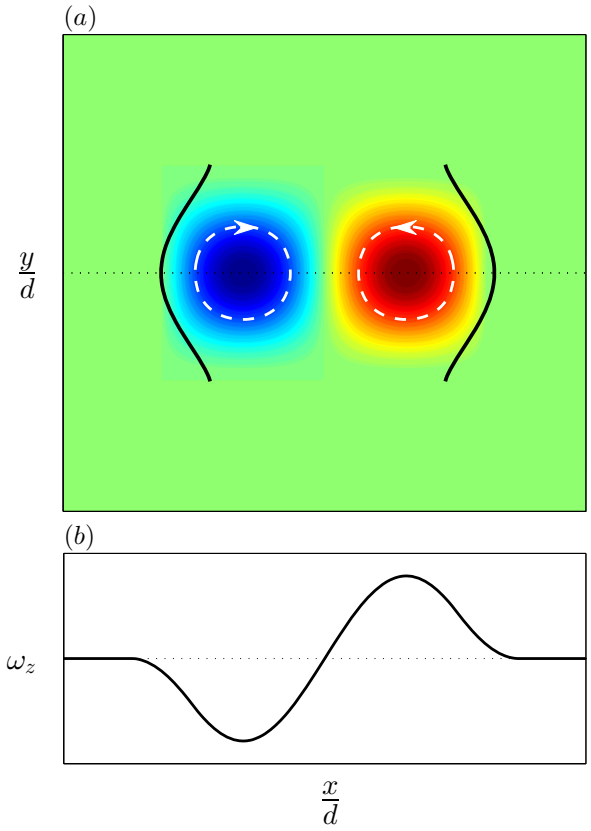

Fig. 11. (a) Schematic interaction of counter-rotating vortices with flame fronts, which are highlighted by black solid curves. (b) Schematic variation of vorticity along the horizontal axis. The variation is presented along the axis passing through the vortices centers, see the dotted line in (a).

terms, that are the first and the third terms on the RHS of Eq. (2), are negligible. As a result, Eq. (2) simplifies to:

$$\frac{\partial \omega_z}{\partial t} + v\frac{\partial \omega_z}{\partial x} + u\frac{\partial \omega_z}{\partial y} = \nu\left(\frac{\partial^2 \omega_z}{\partial x^2} + \frac{\partial^2 \omega_z}{\partial y^2}\right) - \omega_z\left(\frac{\partial v}{\partial x} + \frac{\partial u}{\partial y}\right). \tag{12}$$

It can be shown that the vorticity function that satisfies Eq. (12) is an odd function. This means that, for fixed values of t, y, and u, $-v$, $-x$, and $-\omega_z$ satisfy Eq. (12). The ongoing argument suggests that, the heat release causes the vicosity and the dilatation terms on the RHS of both Eqs. (2) and (12) to become dominated. This leads to the vortices to arrange in a symmetric pattern, which causes the symmetry of the flame fronts with respect to the vertical axis.

3.3. Periodicity of the flame front corrugations

The POD technique was utilized to investigate dominant modes of the flame front position signal. The POD technique used in here is similar to that utilized for studying the non-reacting flow characteristics. Specifically, variation of x along the vertical axis is cast into a matrix, given by: $\boldsymbol{x}^i = [x_1^i \; x_2^i \; x_3^i \; \ldots x_M^i]^{\mathrm{T}}$, where the superscript i corresponds to the i^{th} Mie scattering image, and M is the number of data points along the vertical axis, i.e., $M = 1160$. Using $\boldsymbol{x}^i$ along with the mean flame front position ($\overline{\boldsymbol{x}}$), fluctuations of the flame front position signal ($\boldsymbol{x'}^i = \boldsymbol{x}^i - \overline{\boldsymbol{x}}$) were estimated and cast into the following matrix.

$$\boldsymbol{R} = [\boldsymbol{x'}^1 \; \boldsymbol{x'}^2 \; \boldsymbol{x'}^3 \; \ldots \; \boldsymbol{x'}^N] = \begin{bmatrix} x_1'^1 & x_1'^2 & x_1'^3 & \ldots & x_1'^N \\ x_2'^1 & x_2'^2 & x_2'^3 & \ldots & x_2'^N \\ x_3'^1 & x_3'^2 & x_3'^3 & \ldots & x_3'^N \\ \vdots & \vdots & \vdots & \vdots & \vdots \\ x_M'^1 & x_M'^2 & x_M'^3 & \ldots & x_M'^N \end{bmatrix}, \tag{13}$$

where N is the number of acquired Mie scattering images, i.e., $N = 1000$. Using $\boldsymbol{R}$, the autocovarience matrix ($\boldsymbol{S} = \boldsymbol{R}^{\mathrm{T}}\boldsymbol{R}$) was estimated. The eigenvalues (λ^i) and eigenvectors ($\mathbf{G}^i = [g_1^i \; g_2^i \; g_3^i \; \ldots \; g_N^i]^{\mathrm{T}}$) of the autocovarience matrix were estimated by solving the following eigenvalue problem:

$$\mathbf{S}\mathbf{G}^i = \lambda^i \mathbf{G}^i. \tag{14}$$

For all experimental conditions tested, the eigenvalues and the corresponding eigenvectors were obtained from Eq. (14). The eigenvalues were arranged in a descending order and are presented in Fig. 12(a). Using the arguments presented in Epps and Techet [51], see Eq. (5), the threshold eigenvalues pertaining to all experimental conditions were estimated. Specifically, for Flames A,

B, C, D, E, and F, the mode numbers pertaining to the threshold eigenvalue are 8, 6, 32, 12, 27, and 20, respectively. In Fig. 12, results associated with the mode numbers smaller than those obtained from the threshold eigenvalue are highlighted by the corresponding data symbols. The results pertaining to the eigenvalues of the first two modes (λ^1 andλ^2) are enlarged and shown in the inset of Fig. 12(a). As can be seen from the results in the figure, λ is dependent on the experimental conditions tested. Specifically, for the first and the second modes, the results show that increasing the fuel-air equivalence ratio increases λ. However, for the rest of the modes, increasing ϕ decreases the corresponding eigenvalues. Since the eigenvalues are associated with the energy of the flame front position, RMS of this parameter (x_{RMS}) was utilized to investigate influence of the fuel-air equivalence ratio on the first and the second POD modes. Values of x_{RMS} were previously investigated, and the corresponding results were presented in Fig. 9(d-f). As the results presented in the figure show, x_{RMS} increases along the vertical axis. In order to facilitate comparisons, the maximum value of x_{RMS} was utilized for the arguments. This parameter is approximately 0.9, 1.15, 0.5, 0.7, 0.6, and 0.65 mm, for Flames A, B, C, D, E, and F, respectively. Comparison of the results pertaining to the maximum value of x_{RMS} show that increasing ϕ increases maximum value of x_{RMS}, which is similar to the trend associated with influence of ϕ on the first and the second eigenvalues. This argument suggests that increasing the fuel-air equivalence ratio leads to increase in large scale flame front fluctuations, which lead to the increase of the first and the second POD modes of the flame front position.

Values of the normalized cumulative mode energy associated with the experimental conditions presented in Fig. 12(a) are shown in Fig. 12(b). The results in the figure show that increasing the mean bulk flow velocity, which is synonymous with increase of the Reynolds number, decreases the normalized cumulative mode energy. It is speculated that this trend is linked to the background turbulent velocity fluctuations. This is because, on one hand, energy of the background velocity

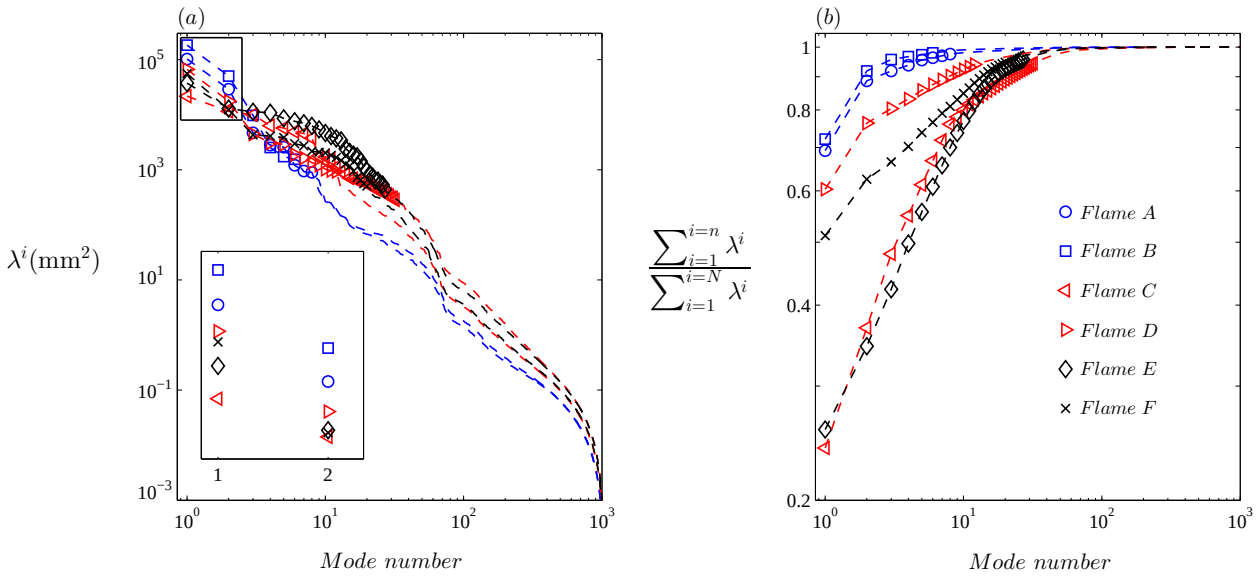

Fig. 12. (a) Variation of the eigenvalue pertaining to flame front position signal. (b) Normalized Cumulative mode energy associated with the results presented in (a).

fluctuations is associated with relatively large mode numbers; and, on the other hand, fluctuations of the flame front position are linked to those of the velocity field. Thus, increasing the Reynolds number increases the background velocity fluctuations, which increases the energy of the flame front position pertaining to large mode numbers. This means that, increase of the Reynolds number distributes the energy of the flame front position in relatively larger number of modes. Thus, for a given mode number, increasing the Reynolds number decreases the cumulative mode energy.

In order to investigate the periodicity of the flame front corrugations, the POD mode shapes were estimated using the following formulation:

$$\boldsymbol{\psi}^i = \frac{\sum_{n=1}^{n=N} g_n^i \boldsymbol{x'}^i}{|\sum_{n=1}^{n=N} g_n^i \boldsymbol{x'}^i|}. \tag{15}$$

Figures 13(a), 13(b), 13(c), and 13(d) presents the first, second, twenty seventh, and one hundredth POD mode shapes associated with Flame E condition. The POD mode shape pertaining to the largest mode number is dominated by uncertainty in estimation of the flame front position signal,

and is highlighted in red. The results in Figs. 13(a-c) show that increasing the mode number increases fluctuations of $\boldsymbol{\psi}$ along the vertical axis. In order to investigate this, normalized power spectrum densities (PSD^*) associated with $\boldsymbol{\psi}^1$ to $\boldsymbol{\psi}^{27}$ were estimated. The values of PSD^* were obtained using the FFT technique. The number of data points utilized for the FFT analysis was selected to be 2^{10}. This leads to a resolution which allows for resolving the dominant wave numbers associated with the corrugations of the flame front, while avoiding noise in the FFT analysis. The results pertaining to the normalized power spectrum densities of the POD mode shapes are presented in Fig. 14. Since the POD mode shapes pertaining to mode numbers larger than 27 are influenced by measurement uncertainty, only results associated with $\boldsymbol{\psi}^1$ to $\boldsymbol{\psi}^{27}$ are presented in the figure. As can be seen, for a given mode number, PSD^* features a dominant peak. The wave number pertaining to the peak, is referred to as κ_c, and features an increasing trend with increasing the POD mode number, which is in agreement with the results presented in Fig. 13.

Values of the dominant wave number (κ_c) pertaining to the results in Fig. 14 are presented in Fig. 15. The uncertainty in estimation of κ_c pertains to the resolution of the spectral analysis and is accommodated by the size of the error bar in the figure. Also shown in the figure is the dominant wave number ($1/l$) pertaining to the non-reacting flow over a circular cylinder. Value of $1/l$ can change approximately by twice of the PIV resolution. This leads to an error in estimation of $1/l$ which is shown by the highlighted region in Fig. 15. The results in the figure suggest that, for Flame E condition, the dominant wave number associated with mode numbers 1-10 of the flame front corrugations matches the dominant wave number pertaining to non-reacting flow over a circular cylinder. Similar results were obtained for the rest of the experimental conditions tested. Specifically, it was obtained that, for Flames A, B, C, D, and F, spectral characteristics of the first 8, 6, 8, 10, and 7 modes match those of the non-reacting flow, respectively. This suggests that, for the experimental conditions tested, the length scale associated with the flame front wrinkling is

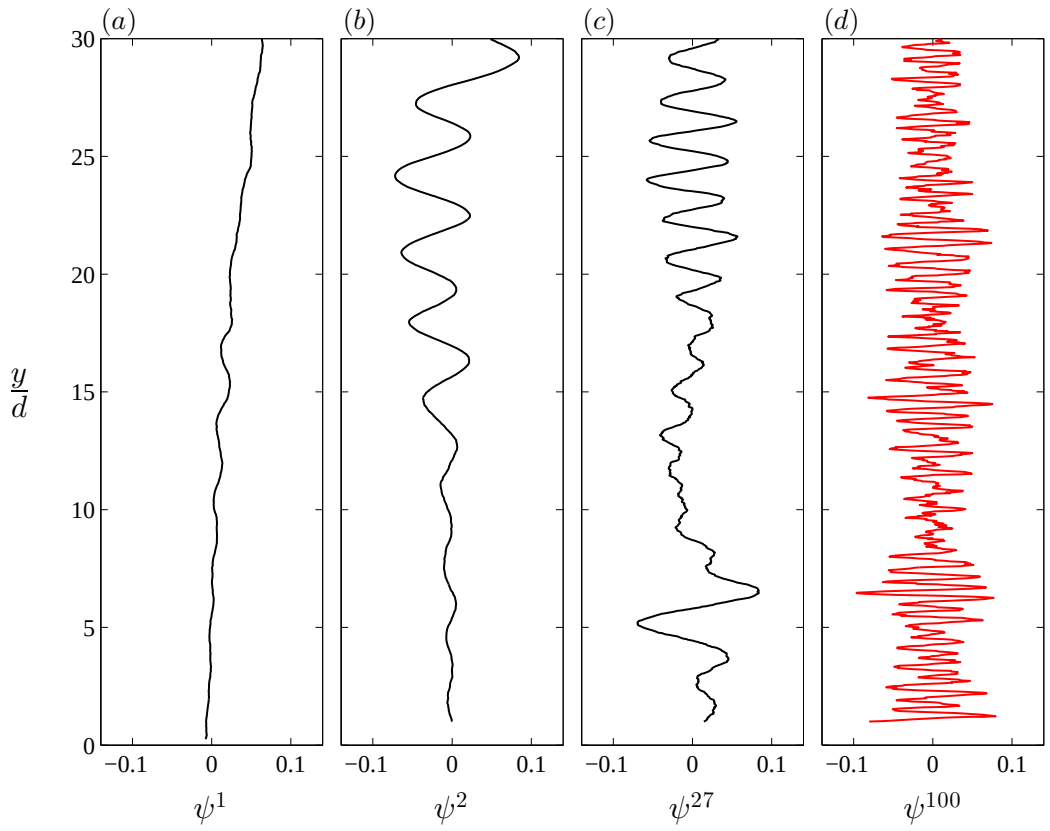

Fig. 13. Mode shapes associated with Flame E condition. (a), (b), (c), and (d) pertain to the first, the second, the twenty seventh, and the one hundredth modes, respectively.

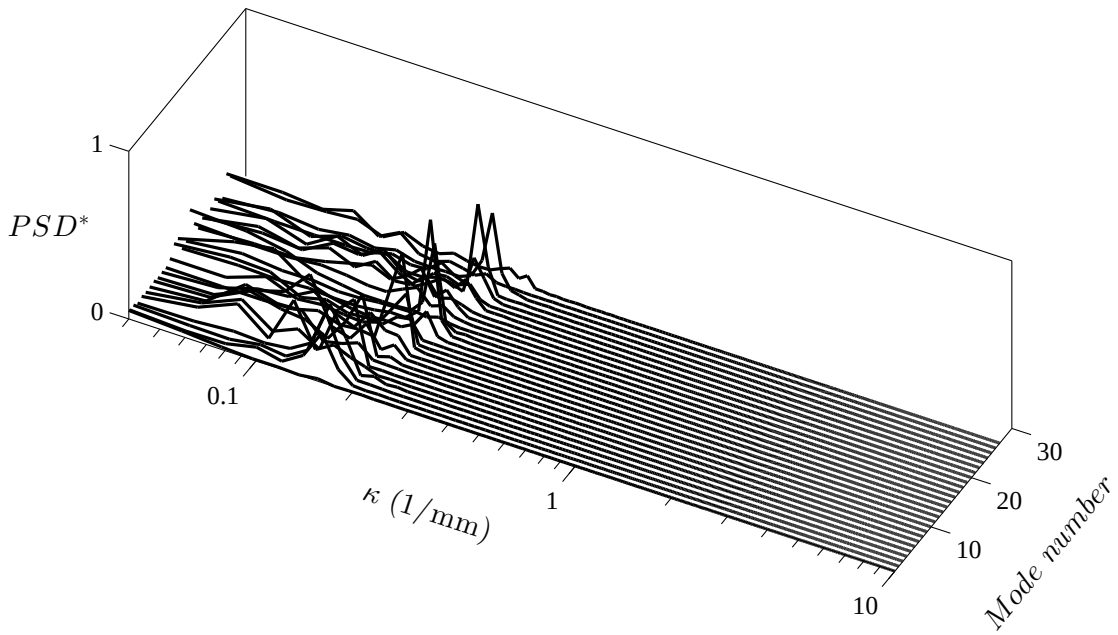

Fig. 14. Normalized power spectrum densities of the mode shapes associated with Flame E condition.

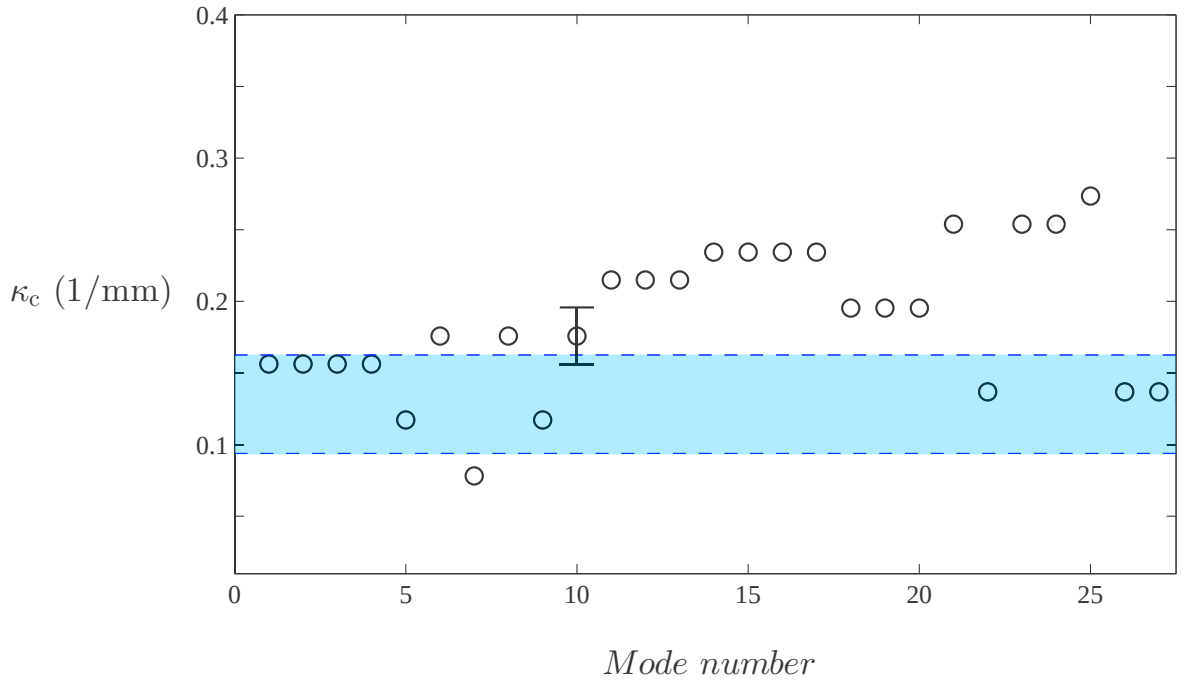

Fig. 15. Variation of the most dominant wave number associated with the results presented in Fig. 14.

similar to the separating distance between vortices associated with non-reacting flow over a circular cylinder.

Comparison of the results presented in this section with those in the previous section may seem to suggest contradictory conclusions. On one hand, the results in previous section showed that the flame fronts are symmetric with respect to the vertical axis. As a results, it was concluded that the vortices are arranged differently from those in the von Kármán vortex street, which suggests that the von Kármán instability is not present for the reacting conditions tested in this study. On the other hand, the length scale associated with the flame surfaces and that pertaining to non-reacting flow over a circular cylinder are similar. The authors believe that this similarity does not necessitate formation of von Kármán vortex street under reacting condition. In fact, past investigations, e.g., Shanbhogue *et al.* [57] show that origin of the vortices which lead to corrugation of the flame surfaces is linked to the shear layer instability formed on both sides of the flame-holder.

Using the POD mode shapes, the flame front position signal was reconstructed utilizing the following formulation:

$$\boldsymbol{x}_{\mathrm{r}}^{i} = \overline{\boldsymbol{x}} + \boldsymbol{\eta}\boldsymbol{\eta}^{\mathrm{T}}\boldsymbol{x}'^{i}, \tag{16}$$

where $\boldsymbol{x}_{\mathrm{r}}$ is the reconstructed flame front position signal and $\boldsymbol{\eta} = [\boldsymbol{\psi}^1\ \boldsymbol{\psi}^2\ \boldsymbol{\psi}^3\ \ldots \boldsymbol{\psi}^m]$. The number of columns of $\boldsymbol{\eta}$ is the number of POD modes utilized for reconstruction of the flame fronts. For the results presented here, Flame E condition was utilized as this condition was extensively studied in previous subsections. However, similar results were obtained for the rest of the experimental conditions tested. For reconstruction of the flame fronts, m was set to 5, 10, and 27. The last two values of m were selected as they correspond to the number of modes that can capture spectral characteristics of the flame front as well as the number of modes that are not significantly influenced by uncertainty of measurements, respectively. In addition to these, results associated with $m = 5$ were considered for comparison purposes. The reconstructed flame fronts pertaining to $m = 5$, 10, and 27 are presented by the red dotted, blue dashed, and green dotted-dashed curves in Fig. 16, respectively. The experimentally obtained flame front, which corresponds to the results presented in Fig. 3, is shown by the solid black curve. An inset of Fig. 16(a) is enlarged and shown in Fig. 16(b). Comparison of the results presented in Fig. 16(b) shows that the the first 10 and 27 modes can capture fluctuations of the flame front. This is in comparison with the results pertaining to $m = 5$, which show that the corresponding reconstructed flame front does not follow the flame front obtained from the Mie scattering images. The arguments provided above suggest that, for Flame E condition, the set of POD modes, with spectral characteristic similar to that pertaining to non-reacting flow over a circular cylinder, can adequately capture fluctuations of the flame front along the vertical axis. In fact, this is the case for all experimental conditions tested in the present study.

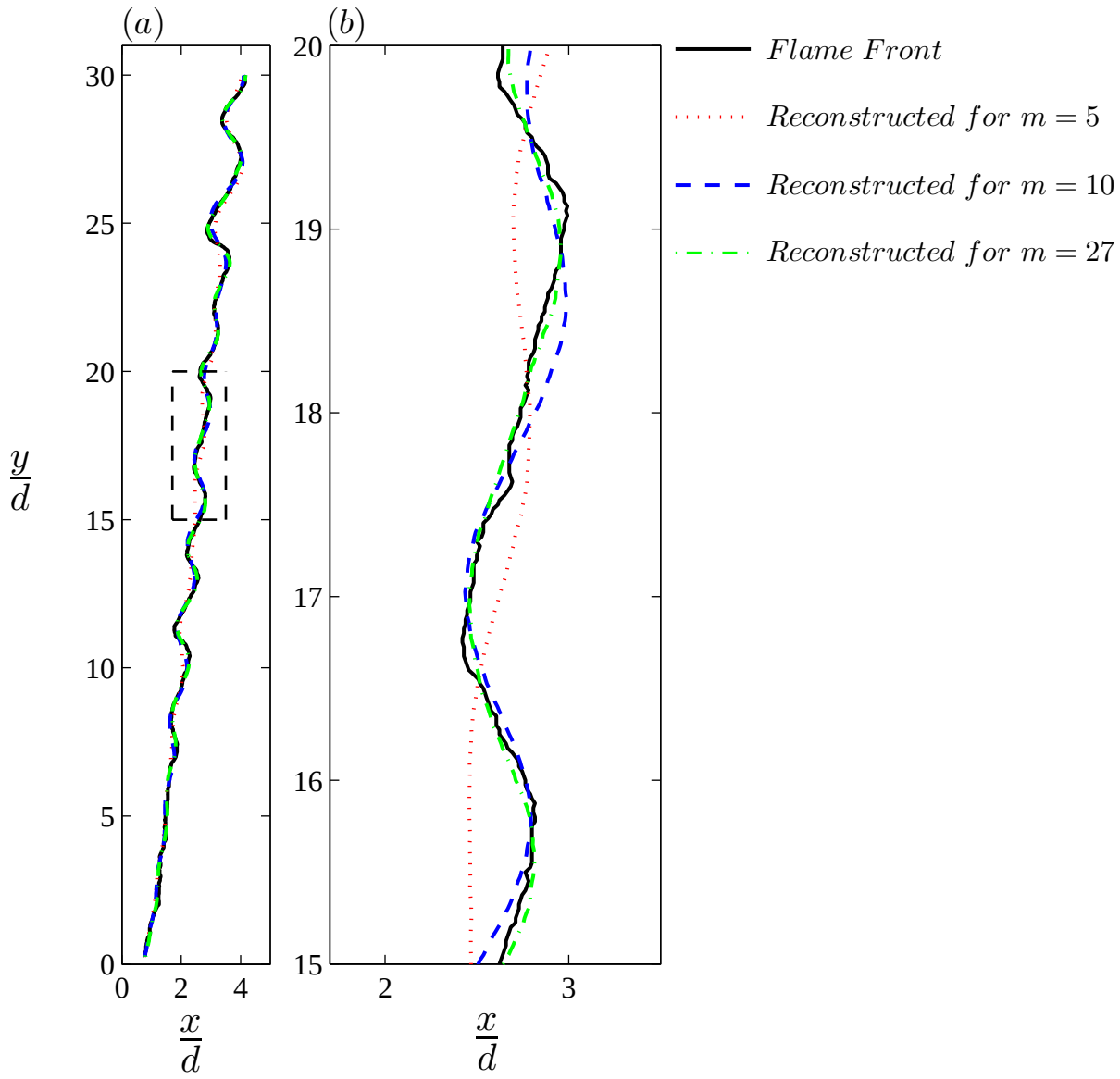

Fig. 16. (a) Reconstruction of the flame front position signal associated with the results presented in Fig. 3(a). (b) is the inset of (a).

Using the required number of POD modes for reconstruction of the flame fronts, it can be shown that Eq. (16) simplifies to:

$$\boldsymbol{x}_{\mathrm{r}}^{i} \approx \overline{\boldsymbol{x}} + \sum_{j=1}^{j=10} b_j^i \boldsymbol{\psi}^j, \tag{17}$$

where b_j^i is referred to as the j^{th} temporal coefficient for reconstruction of the i^{th} flame front position signal. In Eq. (17), the upper bound of summation is associated with the maximum number of modes pertaining to Flame E condition. Following the above arguments, the upper bound of summation for Flames A, B, C, D, and F, are 8, 6, 8, 10, and 7, respectively. It was previously argued that spectral characteristics of $\boldsymbol{\psi}^j$ is similar to that of non-reacting flow. It is of interest to compare the characteristics of the first and the second temporal coefficients associated with the non-reacting flow (a_1 and a_2) with those pertaining to flame front fluctuations (b_1 and b_2). Figure 17(a) shows variation of the normalized temporal coefficients pertaining to the flame front fluctuations for all flame front position signals associated with Flame E condition. As can be seen from the results in the figure, the normalized coefficients are distributed in the plane of $b_1 - b_2$ with most of the data points positioned relatively close to the origin. For flame front position signals with relatively small values of b_1 and b_2, most of the energy is distributed between relatively large number of modes. As a result, fluctuations of the flame front signal along the vertical axis are expected to feature a relatively small wave number. In comparison to the energy of the flame front position signals with relatively small values of b_1 and b_2, energy of those associated with relatively large values of b_1 and/or b_2 is mostly distributed in smaller number of modes. Thus, the corresponding fluctuations of the flame front position signal is expected to feature a relatively smaller wave number. In order to assess this, two representative data points were selected and highlighted in Fig. 17(a). One point is positioned relatively close to the origin, highlighted by the blue solid circular data point; and the other point is positioned relatively far from the origin, highlighted by the red solid circular data

point. Fluctuations of the flame front position pertaining to the blue and the red data points are shown by the blue solid and the red dashed curves in Fig. 17(b), respectively. For clarity purposes, the scale of the horizontal axis is selected to be larger than that of the vertical axis. Normalized power spectrum densities associated with the results in Fig. 17(b) are presented in Fig. 17(c). As can be seen from the results in Fig. 17(c), the dominant wave number associated with the solid curve is larger than that pertaining to the dashed curve. This means that the energy of the flame front position associated with the solid curve, in comparison to that pertaining to dashed curve, is distributed in larger mode numbers. Thus, in agreements with the results in Fig. 17(a), the first two POD coefficients associated with the solid curve are positioned closer to the origin in comparison to the coefficients corresponding to the dashed curve.

Comparison of the results presented in Fig. 17(a) with those in Fig. 7(c) shows that the relation between the first and the second temporal coefficients associated with the flame front position and the velocity data do not follow a similar trend. Specifically, results associated with the velocity data showed that the coefficients are positioned around a unity radius circle; however, those associated with the flame front fluctuations are mainly positioned close to the origin. The reason for this is speculated to be linked to the relative energy of the first and the second POD modes. In order to investigate this, the ratio of the eigenvalues normalized by the first mode eigenvalue are presented in Fig. 18. The results in the figure are extracted from Figs. 4(a) and 12(a). Specifically, the result pertaining to the flame front position and the velocity data are shown by the dashed and dotted-dashed curves, respectively. Schematics of the normalized first and the second temporal coefficients distributions pertaining to the flame front position and the velocity data are presented in Figs. 18(b) and 18(c), respectively. These figures mimic the distributions previously presented in Figs. 17(c) and 7(c). The results in Fig 18 suggest that, increasing the ratio of the second to the first eigenvalue transitions the distribution of the first and the second

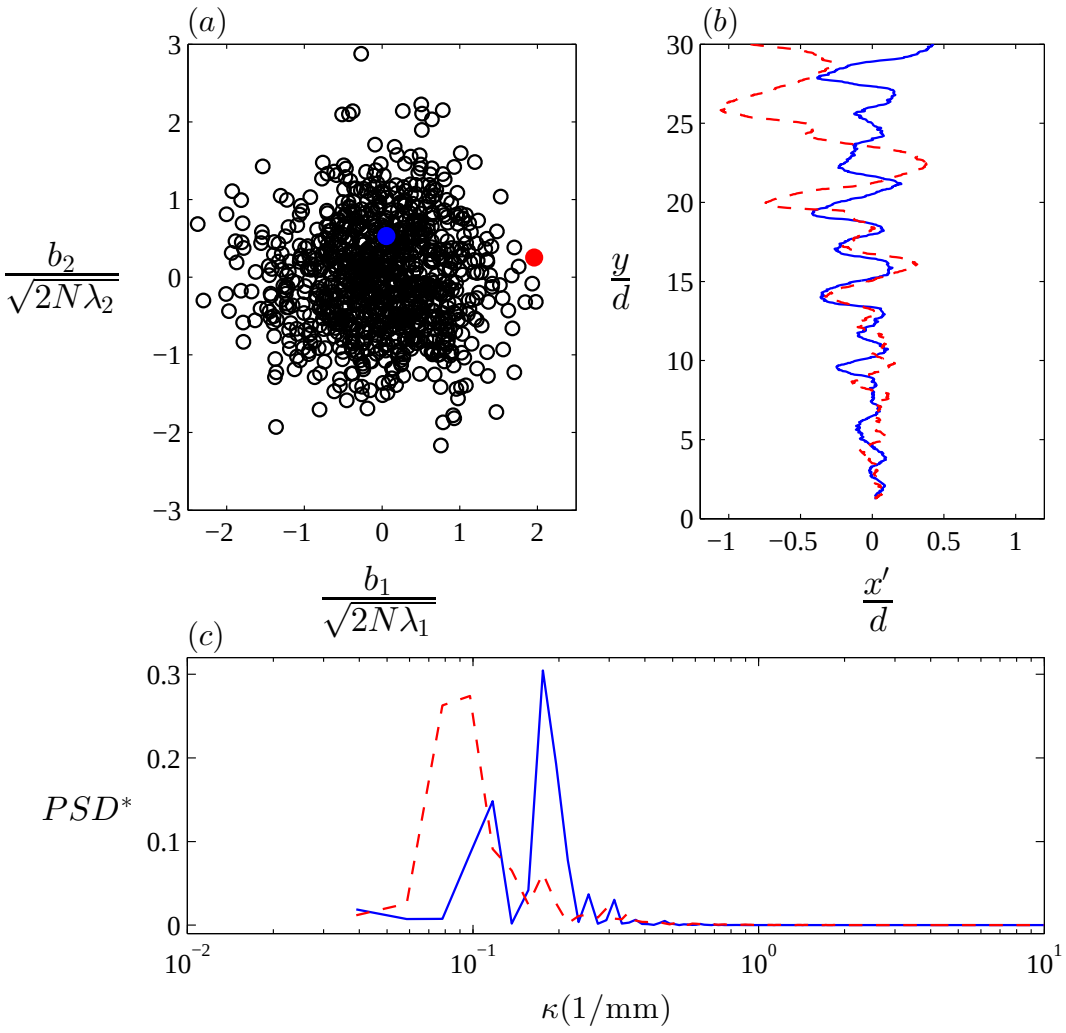

Fig. 17. (a) Variation of the normalized second POD coefficient versus the first POD coefficient associated with Flame E condition. (b) Fluctuations of the flame front position signal along the vertical axis. The blue solid curve pertains to the highlighted data point positioned close to the origin in (a). The red dashed curve corresponds to the data point positioned at a relatively large distance from the origin in (a). (c) Normalized power spectrum densities pertaining to the results presented in (b).

temporal coefficients from a distribution populated at the origin to that populated around a unity radius circle centered at the origin. In order to assess the underlying reason, flame front signals with sinusoidal fluctuations were produced. Specifically, 1000 signals were generated with a wavelength of fluctuations identical to that of Flame E condition and with random phase difference between the signals. Then, corresponding normalized eigenvalues were estimated and the results were presented by the solid line in Fig. 18(a). The corresponding normalized temporal coefficients were obtained and presented in Fig. 18(c). As can be seen from the results in the figure, for sinusoidal fluctuations, the ratio of the second to the first eigenvalues is close to unity and the normalized second and first temporal coefficients are positioned at a unity radius circle. This confirms the conclusion made earlier. That is decreasing λ^2/λ^1 transitions the distribution of the normalized first and second temporal coefficients from a unity radius circle to a distribution which is substantially populated close to the origin.

4. Concluding Remarks

Underlying reasons associated with periodicity in corrugations of weakly turbulent premixed V-shaped flames were investigated experimentally. The experiments were conducted using the Mie scattering as well as the Particle Image Velocimetry techniques. All experiments were performed for relatively small value of background turbulence intensity, i.e., $u_{\mathrm{RMS}}/U \approx 0.02$. Three Reynolds numbers of 510, 790, and 1057 along with two fuel-air equivalence ratios of 0.6 and 0.7 were tested in the experiments.

The results show that the flame fronts are symmetric with respect to the vertical axis and are periodically corrugated in the space domain. Using the vorticity transport equation, the underlying reason associated with the former observation was argued to be linked to the vorticity being an odd function. The characteristics of periodicity in corrugations of the flame fronts were studied

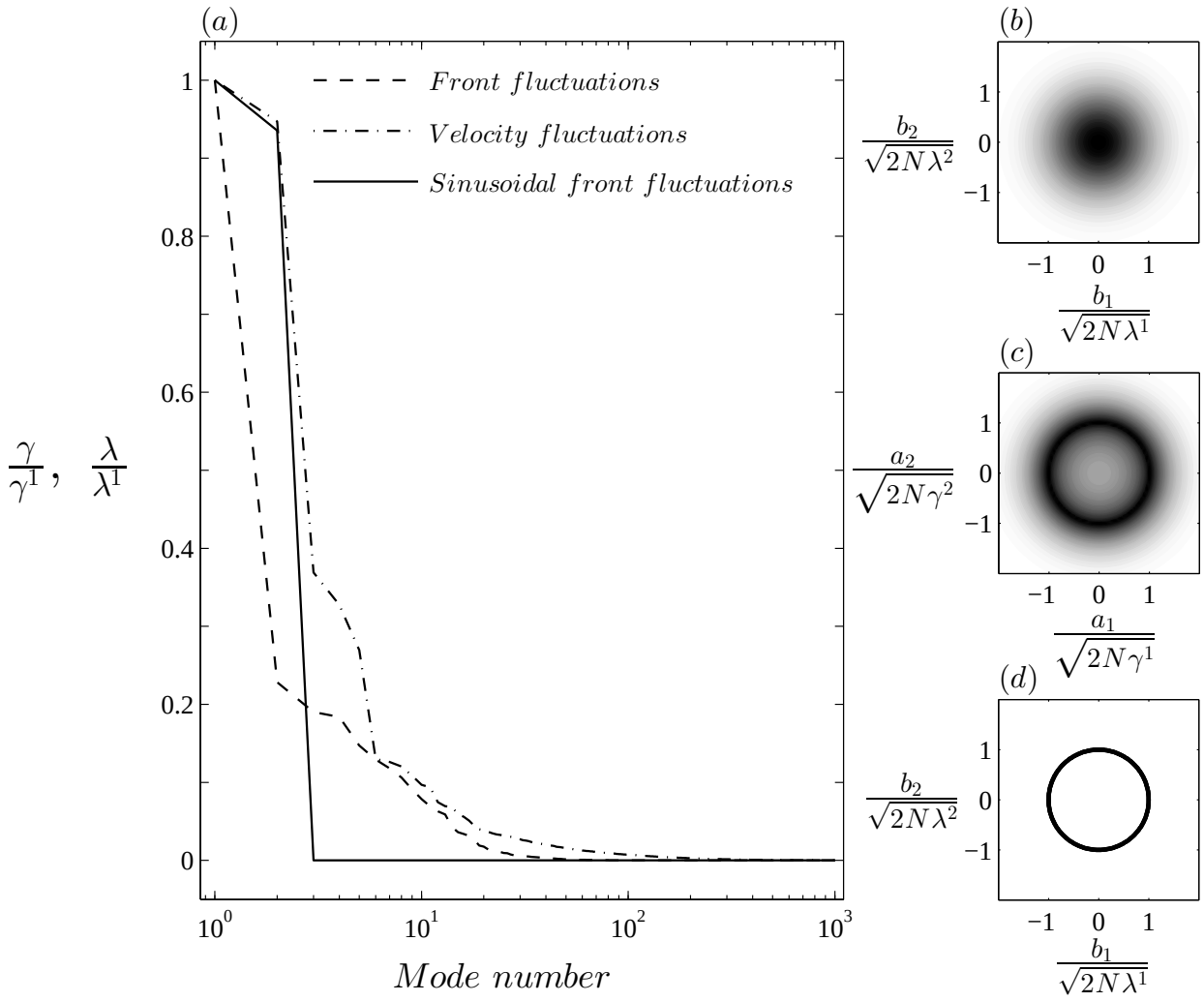

Fig. 18. (a) Normalized eigenvalues of the flame front position signal and the velocity data. The results pertain to Flame E condition. Also presented in the figure is the normalized eigenvalue of sinusoidal flame front fluctuations. (b), (c), and(d) are schematics of the normalized temporal coefficient distributions associated with flame front fluctuations, velocity data, and sinusoidal flame front fluctuations, respectively.

using the Proper Orthogonal Decomposition (POD) technique. The POD analysis show that the velocity data feature a dominant instability, with corresponding normalized wave number being approximately equal to the Strouhal number. Analysis of the results pertaining to fluctuations of the flame front position show that relatively large number of the corresponding POD modes are dominated by an instability, with the pertaining wave number being similar to that associated with the velocity data. This suggests the length scale of the flame front fluctuations is dictated by characteristics of non-reacting flow over a circular cylinder.

Although comparison of the length scales associated with non-reacting flow over a circular cylinder and flame front corrugations feature similar trends, the pertaining POD temporal coefficients are significantly different. Specifically, for the flame front position data, the results show that the normalized coefficients are mainly positioned close to the origin; whereas, those associated with the velocity data are positioned around a unity radius circle centered at the origin. The underlying reason was argued to be linked to the ratio of the second and first pertaining eigenvalues. Specifically, it was argued that increasing this ratio causes the energy of the corresponding signal to become distributed mainly between the first and the second POD modes, leading to distribution of the first and the second temporal coefficients around a circle.

Acknowledgements

The authors are grateful for financial support from the Natural Sciences and Engineering Research Council (NSERC) of Canada as well as the Ontario Graduate Scholarship (OGS) program.

References

[1] N. Peters, Turbulent combustion, 1st Edition, Cambridge University Press, 2000.

[2] I. Glassman, R. A. Yetter, Combustion, 4th Edition, Elsevier Inc., 2008.

[3] P. Clavin, Dynamic behavior of premixed flame fronts in laminar and turbulent flows, Progress in Energy and Combustion Science 11 (1985) 1–59.

[4] A. N. Lipatnikov, J. Chomiak, Turbulent flame speed and thickness: phenomenology, evaluation, and application in multi-dimensional simulations, Progress in Energy and Combustion Science 28 (2002) 1–74.

[5] J. F. Driscoll, Turbulent premixed combustion: Flamelet structure and its effect on turbulent burning velocities, Progress in Energy and Combustion Science 34 (2008) 91–134.

[6] R. K. Cheng, T. T. Ng, On defining the turbulent burning velocity in premixed V-shaped turbulent flames, Combustion and Flame 57 (1984) 155–167.

[7] P. Goix, P. Paranthoen, M. Trinite, A tomographic study of measurements in a V-shaped H_2-air flame and a Lagrangian interpretation of the turbulent flame brush evolution, Combustion and Flame 81 (1990) 229–241.

[8] S. Kheirkhah, Ö. L. Gülder, Topology and brush thickness of turbulent premixed V-shaped flames, Flow, Turbulence and Combustion 93 (2014) 439–459.

[9] S. J. Shanbhogue, Dynamics of perturbed exothermic bluff-body flow-fields, Ph.D. thesis, Georgia Institute of Technology, Atlanta, GA (2008).

[10] R. E. Petersen, H. W. Emmons, Stability of laminar flames, Physics of Fluids 4 (1961) 456.

[11] E. Berger, R. Wille, Periodic flow phenomena, Annual Review of Fluid Mechanics 11 (1972) 313–340.

[12] P. W. Bearman, Vortex shedding from oscillating bluff bodies, Annual Review of Fluid Mechanics 16 (1984) 195–222.

[13] H. Choi, W. Jeon, J. Kim, Control of flow over a bluff body, Annual Review of Fluid Mechanics 40 (2008) 113–139.

[14] C. H. K. Williamson, Vortex dynamics in the cylinder wake, Annual Review of Fluid Mechanics 28 (1996) 477–539.

[15] M. M. Zdravkovich, Flow around circular cylinders: Fundamentals, Vol. 1, Oxford University Press, 1997.

[16] C. Norberg, Fluctuating lift on a circular cylinder: review and new measurements, Journal of Fluids and Structures 17 (2003) 57–96.

[17] J. H. Gerrard, The wakes of cylindrical bluff bodies at low Reynolds number, Philosophical Transactions of the Royal Society of London. Series A, Mathematical and Physical Sciences 288 (1978) 351–382.

[18] A. Roshko, Experiments on the flow past a circular cylinder at very high Reynolds number, Journal of Fluid Mechanics 10 (1961) 345–356.

[19] P. W. Bearman, On vortex shedding from a circular cylinder in the critical Reynolds number regime, Journal of Fluid Mechanics 37 (1969) 577–585.

[20] C. M. Coat, Coherent structures in combustion, Progress in Energy and Combustion Science 22 (1996) 427–509.

[21] S. J. Shanbhogue, S. Husain, T. Lieuwen, Lean blowoff of bluff body stabilized flames: Scaling and dynamics, Progess in Energy and Combustion Science 35 (2009) 98–120.

[22] R. R. Erickson, M. C. Soteriou, P. G. Mehta, The influence of temperature ratio on the dynam-

ics of bluff body stabilized flames, Paper 753 (2006) in 44th AIAA aerospace sciences meeting and exhibit.

[23] S. M. Bush, E. J. Gutmark, Reacting and non-reacting flow fields of a V-gutter stabilized flame, AIAA Journal 45 (2007) 662–672.

[24] J. R. Hertzberg, I. G. Shepherd, L. Talbot, Vortex shedding behind rod stabilized flames, Combustion and Flame 86 (1991) 1–11.

[25] S. Yamaguchi, N. Ohiwa, T. Hasegawa, Structure and blow-off mechanism of rod-stabilized premixed flame, Combustion and Flame 62 (1985) 31–41.

[26] J. R. G. Bill, K. Tarabanis, The effect of premixed combustion on the recirculation zone of circular cylinders, Combustion Science and Technology 47 (1986) 39–53.

[27] C. N. Cross, Combustion heat release effects on asymmetric vortex shedding from bluff bodies, Ph.D. thesis, Georgia Institute of Technology, Atlanta, GA (2011).

[28] C. Smith, D. Nickolaus, T. Leach, B. Kiel, K. Garwick, LES blowout analysis of premixed flow past V-gutter flameholder, Paper 170 (2007) in 45th AIAA aerospace sciences meeting and exhibit.

[29] A. C. Eckbreth, Laser diagnostics for combustion temperature and species, 2nd Edition, Overseas Publishers Association, 1996.

[30] J. R. Hertzberg, M. Namazian, L. Talbot, A laser tomographic study of a laminar flame in a Kármán vortex street, Combustion Science and Technology 38 (1984) 205–216.

[31] K. Atashkari, M. Lawes, C. G. W. Sheppard, R. Woolley, Towards a general correlation of turbulent premixed flame wrinkling, in: Proceedings of the 4th International Symposium on

Engineering Turbulence Modelling and Measurements, Engineering Turbulence Modelling and Experiments - 4 W. Rodi and D. Laurence (Editors), ISBN0 08 043328 6, 1999, pp. 805–814.

[32] D. C. Bingham, F. C. Gouldin, D. A. Knaus, Crossed-plane laser tomography: Direct measurement of the flamelet surface normal, Twenty-seventh Symposium (International) on Combustion/ The Combustion Institute (1998) 77–84.

[33] J. B. Bell, M. S. Day, I. G. Shepherd, M. R. Johnson, R. K. Cheng, J. F. Grcar, V. E. Beckner, M. J. Lijewski, Numerical simulation of a laboratory-scale turbulent V-flame, Proceedings of the National Academy of Sciences of the United States of America 102 (29) (2005) 10006–10011.

[34] P. C. Miles, F. C. Gouldin, Mean reaction rates and flamelet statistics for reaction rate modelling in premixed turbulent flames, Proceedings of the Combustion Institute 24 (1992) 477–484.

[35] D. A. Knaus, F. C. Gouldin, Measurements of flamelet orientations in premixed flames with positive and negative Markstein numbers, Proceedings of the Combustion Institute 28 (2000) 367–373.

[36] S. S. Sattler, D. A. Knaus, F. C. Gouldin, Determination of three-dimensional flamelet orientation distributions in turbulent V-flames from two-dimensional image data, Proceedings of the Combustion Institute 29 (2002) 1785–1792.

[37] S. Kheirkhah, Ö. L. Gülder, Turbulent premixed combustion in V-shaped flames: characteristics of flame front, Physics of Fluids 25 (2013) 055107.

[38] N. Peters, Laminar flamelet concepts in turbulent combustion, Proceedings of the Combustion Institute 21 (1986) 1231–1250.

[39] G. J. Smallwood, Ö. L. Gülder, D. R. Snelling, B. M. Deschamps, I. Gökalp, Characterization

of flame front surfaces in turbulent premixed methane/air combustion, Combustion and Flame 101 (1995) 461–470.

[40] Ö. L. Gülder, Contribution of small scale turbulence to burning velocity of flamelets in the thin reaction zone regime, Proceedings of the Combustion Institute 31 (2007) 1369–1375.

[41] P. C. Miles, Conditional velocity statistics and time-resolved flamelet statistics in premixed turbulent v-shaped flames, Ph.D. thesis, Cornell University, Ithaca, NY (1991).

[42] T. W. Lee, G. L. North, D. L. Santavicca, Surface properties of turbulent premixed propane/air flames at various Lewis numbers, Combustion and Flame 93 (1993) 445–456.

[43] W. L. Roberts, J. F. Driscoll, M. C. Drake, L. P. Goss, Images of quenching of a flame by a vortex-to quantify regimes of turbulent combustion, Combustion and Flame 94 (1993) 58–69.

[44] G. Yu, C. K. Law, C. K. Wu, Laminar flame speeds of hydrocarbon + air mixtures with hydrogen addition, Combustion and Flame 63 (1986) 339–347.

[45] S. B. Pope, Turbulent flows, Cambridge University Press, 2000.

[46] J. L. Lumley, Stochastic tools in turbulence, New York: Academic Press, 1972.

[47] G. Berkooz, P. Holmes, J. L. Lumley, The proper orthogonal decomposition in analysis of turbulent flows, Annual Review of Fluid Mechanics 25 (1993) 539–575.

[48] K. E. Meyer, P. J. M., Özcan O., A turbulent jet in cross flow analysed with proper orthogonal decomposition, Journal of Fluid Mechanics 583 (2007) 199–227.

[49] L. Kourentis, E. Konstantinidis, Uncovering large-scale coherent structures in natural and forced turbulent wakes by combining PIV, POD, and FTLE, Experiments in Fluids 52 (2011) 749–763.

[50] R. Perrin, M. Braza, E. Cid, S. Cazin, A. Barthet, A. Sevrain, C. Mockett, F. Thiele, Obtaining phase averaged turbulence properties in the near wake of a circular cylinder at high Reynolds number using POD, Experiments in Fluids 43 (2007) 341–355.

[51] B. P. Epps, A. H. Techet, An error threshold criterion for singular value decomposition modes extracted from PIV data, Experiments in Fluids 48 (2010) 355–367.

[52] T. K. Sengupta, N. Singh, V. K. Suman, Dynamical system approach to instability of flow past a circular cylinder, Journal of Fluid Mechanics 656 (2010) 82–115.

[53] T. Ruiz, C. Sicot, L. E. Brizzi, J. Borée, Y. Geravis, Pressure/velocity coupling induced by a near wall wake, Experiments in Fluids 49 (2010) 147–165.

[54] B. W. van Oudheusden, F. Scarano, N. P. van Hinsberg, D. W. Watt, Phase-resolved characterization of vortex shedding in the near wake of a square-section cylinder at incidence, Experiments in Fluids 39 (2005) 86–98.

[55] T. K. Sengupta, S. I. Haider, M. K. Parvathi, G. Pallavi, Enstrophy-based proper orthogonal decomposition for reduced-order modeling of flow past a cylinder, Physical Review E 91 (2015) 043303.

[56] R. Bracewell, The Fourier transform and its applications, New York: McGraw-Hill, 1986.

[57] S. J. Shanbhogue, D. H. Shin, S. Hemchandra, D. Plaks, T. Lieuwen, Flame sheet dynamics of bluff-body stabilized flame during longitudinal acoustic forcing, Proceedings of the Combustion Institute 32 (2009) 1787–1794.